



HAL
open science

Accurate proper motions of the protostellar binary system L 1551 IRS 5

Ricardo Hernández Garnica, Laurent Loinard, Aurora Duran, Jazmín Ordóñez-Toro, Claire J Chandler, Sergio A Dzib, Nicolás Cuello, François Ménard, María José Maureira, Eleonora Bianchi, et al.

► **To cite this version:**

Ricardo Hernández Garnica, Laurent Loinard, Aurora Duran, Jazmín Ordóñez-Toro, Claire J Chandler, et al. Accurate proper motions of the protostellar binary system L 1551 IRS 5. Monthly Notices of the Royal Astronomical Society, 2024, 535 (4), pp.2948 - 2969. 10.1093/mnras/stae2482 . hal-04810888

HAL Id: hal-04810888


















<https://hal.science/hal-04810888v1>

Submitted on 29 Nov 2024

HAL is a multi-disciplinary open access archive for the deposit and dissemination of scientific research documents, whether they are published or not. The documents may come from teaching and research institutions in France or abroad, or from public or private research centers.

L'archive ouverte pluridisciplinaire **HAL**, est destinée au dépôt et à la diffusion de documents scientifiques de niveau recherche, publiés ou non, émanant des établissements d'enseignement et de recherche français ou étrangers, des laboratoires publics ou privés.

Accurate proper motions of the protostellar binary system L 1551 IRS 5

Ricardo Hernández Garnica ^{1,★}, Laurent Loinard ^{1,2,3}, Aurora Duran ¹, Jazmín Ordóñez-Toro ¹,
 Claire J. Chandler ⁴, Sergio A. Dzib ⁵, Nicolás Cuello ⁶, François Ménard ⁶,
 María José Maureira ⁷, Eleonora Bianchi ⁸, Fernando Cruz-Sáenz de Miera ⁶,
 Carlos Carrasco-González ¹, Luis F. Rodríguez ¹, Rosa M. Torres ⁹, Alejandro C. Raga ¹⁰,
 Jeremy Lim ¹¹ and Anton Feeny-Johansson ¹²

¹Instituto de Radioastronomía y Astrofísica, Universidad Nacional Autónoma de México, Apartado Postal 3-72, Morelia 58090, Michoacán, Mexico

²Black Hole Initiative at Harvard University, 20 Garden Street, Cambridge, MA 02138, USA

³David Rockefeller Center for Latin American Studies, Harvard University, 1730 Cambridge Street, Cambridge, MA 02138, USA

⁴National Radio Astronomy Observatory, PO Box O, Socorro, NM 87801, USA

⁵Max-Planck-Institut für Radioastronomie, Auf dem Hügel 69, D-53121 Bonn, Germany

⁶Université Grenoble Alpes, CNRS, Institut de Planétologie et d'Astrophysique / Unité Mixte de Recherche 5274, F-38000 Grenoble, France

⁷Max-Planck-Institut für extraterrestrische Physik (MPE), Gießenbachstraße 1, D-85741 Garching bei München, Germany

⁸Excellence Cluster ORIGINS, Boltzmannstraße 2, D-85748 Garching bei München, Germany

⁹Departamento de Física, CUCEI, Universidad de Guadalajara, Boulevard Marcelino García Barragán 1421, Olímpica, Guadalajara 44430, Jalisco, México

¹⁰Instituto de Ciencias Nucleares, Universidad Nacional Autónoma de México, Apartado Postal 70-543, 04510 Ciudad de México, Mexico

¹¹Department of Physics, The University of Hong Kong, Pokfulam Road, Hong Kong

¹²National Astronomical Observatory of Japan, Osawa 2-21-1, Mitaka, Tokyo 181-8588, Japan

Accepted 2024 October 24. Received 2024 October 22; in original form 2024 September 19

ABSTRACT

We present an extensive astrometric study of the protostellar binary system L 1551 IRS 5, utilizing nearly four decades of interferometric observations obtained between 1983 and 2022 with the *Karl G. Jansky* Very Large Array (VLA) and the Atacama Large Millimeter/submillimeter Array (ALMA). We focus on observations with sufficient angular resolution to separate the two protostars (L 1551 IRS 5 N and S) in the system and derive accurate absolute proper motions for the two sources, as well as the relative proper motion between them. The absolute proper motion is dominated by the solar motion with only a modest contribution from L 1551 IRS 5's peculiar velocity, as expected for a young stellar object. The relative proper motions enable us to constrain the orbit and derive a total mass of $0.96 \pm 0.17 M_{\odot}$ for the system. While the emission of both sources at wavelengths shorter than about 1.3 cm is compact, the emission at longer wavelengths ($\lambda \gtrsim 2$ cm) is often affected by a free-free contribution from nearby shock features. The results presented here demonstrate that, when appropriate care is taken to combine the observations, interferometric data collected with different facilities, at different frequencies, and with different gain calibrators can be combined to obtain accurate astrometry. Observations of L 1551 IRS 5 over the next several decades with the VLA, ALMA, and eventually the ngVLA and SKA ought to improve its dynamical mass measurement down to an accuracy of a few per cent. Similar observations of other young multiple systems have the unique potential to provide dynamical mass estimates for the youngest known stellar objects.

Key words: astrometry – proper motions – (stars:) binaries: general – stars: formation – stars: protostars.

1 INTRODUCTION

Large conventional radio interferometers such as the *Karl G. Jansky* Very Large Array (VLA) or the Atacama Large Millimeter/submillimeter Array (ALMA) can routinely provide astrometric measurements with an accuracy of the order of 10 milliarcsec (mas–Loinard 2002; Rodríguez et al. 2003a; Chandler et al. 2005; Loinard et al. 2007; Dzib et al. 2017; Hernández-Gómez et al. 2019; Maureira et al. 2020). While inadequate to constrain trigonometric

parallaxes, except for the nearest stars, such accuracy is sufficient for the measurements of proper motion of the order of 1 mas yr^{-1} provided the targets of interest are monitored for a decade or more. Combined with well-constrained distances and with radial velocities obtained from spectroscopic measurements, accurate proper motions enable the determination of the six components of the phase space coordinates of the target. This information can be used to constrain the kinematics of sources of interest in the Galactic potential and in their more local environment. For instance, Rivera et al. (2015) used radio astrometry to examine the internal kinematics of the Taurus star-forming region as well as the relative motion between the Taurus and Ophiuchus complexes. In binary or multiple stellar systems, proper

* E-mail: r.hernandezg@irya.unam.mx

motion measurements can be used to constrain the orbital paths and, through Kepler’s law, stellar masses (e.g. Maureira et al. 2020).

Achieving accurate astrometry with radio interferometers requires accounting for a number of issues. First, several emission mechanisms can contribute in varying proportions to the emission at different wavelengths (e.g. Rodríguez et al. 1998), so it is important to make sure that the positions measured in each observation trace the same physical object. For instance, in the case of young stellar systems, compact millimetre emission will typically trace discs while centimetre emission could trace jets and shocks. A second issue to consider is that, for interferometers, the astrometric information is encoded as a visibility phase term (Reid & Honma 2014) which is calibrated against a nearby quasar used as astrometric reference, i.e. the *phase* or *gain* calibrator. Since the absolute positions of these quasars have finite accuracy, combining observations obtained with different gain calibrators can lead to systematic astrometric errors. Finally, astrometric errors could also be introduced if data from instruments using different phase calibration strategies are combined.

Here, we focus on the young stellar system L 1551 IRS 5, located in the Taurus star-forming complex (Strom, Strom & Vrba 1976). The distance to the dark cloud Lynds 1551 (Lynds 1962), which we will adopt as representative of L 1551 IRS 5 itself, has been measured to be 146.4 ± 0.5 pc (Galli et al. 2018, 2019). L 1551 IRS 5 is a Class I binary system (Adams, Lada & Shu 1987) currently oriented roughly in the north–south direction (Bieging & Cohen 1985; Looney, Mundy & Welch 1997). The two stars comprising the system are called L 1551 IRS 5 N (North) and L 1551 IRS 5 S (South); each is surrounded by a compact circumstellar disc (e.g. Rodríguez et al. 1998; Looney, Mundy & Welch 2000; Lim & Takakuwa 2006) and, together, they are surrounded by a circumbinary disc (Cruz-Sáenz de Miera et al. 2019; Takakuwa et al. 2020) and an extended envelope (Looney et al. 2000; Bianchi et al. 2020). The circumstellar and circumbinary discs are all approximately coplanar (Rodríguez et al. 1998; Lim & Takakuwa 2006; Cruz-Sáenz de Miera et al. 2019; Takakuwa et al. 2020). Two radio jets, roughly parallel to each other and perpendicular to the circumstellar discs, are driven by the two protostars in L 1551 IRS 5 (Rodríguez et al. 2003b); they connect on larger scales with optical counterparts and Herbig–Haro objects (Fridlund & Liseau 1998; Itoh et al. 2000; Hayashi & Pyo 2009). The relative orientation of the discs and jets strongly suggest that the binary system L 1551 IRS 5 was formed as a result of disc fragmentation (Lim & Takakuwa 2006; Lim et al. 2016).

The astrometry of the L 1551 IRS 5 system was first studied by Rodríguez et al. (2003a) who used four VLA observations obtained at $\nu = 15$ GHz over a period of about 15 yr (1983 to 1998). Assuming a circular orbit inclined by 60° and oriented exactly in the north–south direction, Rodríguez et al. (2003a) found that the relative astrometry between the sources implies an orbital period $P \approx 260$ yr, a semimajor axis $a \approx 45$ au, and a total mass for the system of the order of $M_{\text{tot}} \approx 1.3 M_\odot$.¹ Rodríguez et al. (2003a) also considered the absolute proper motion of the individual stars in L 1551 IRS 5, but used only three of the four epochs for that purpose as the remaining epoch used a different gain calibrator. Villa et al. (2017) performed a very similar study by using six VLA observations obtained at $\nu = 45$ GHz distributed over a period of 16 yr (1997 to 2012). Following a treatment rigorously analogous to that of Rodríguez et al. (2003a), they obtained an orbital period $P \approx 246$

yr, a semimajor axis $a \approx 49$ au, and a total mass for the system of the order of $M_{\text{tot}} \approx 1.9 M_\odot$.¹ Villa et al. (2017) also considered absolute proper motions, but their results are somewhat inconclusive because two different gain calibrators were used during the observations. To extend the time coverage, Lim & Takakuwa (2006) combined the four observations at $\nu = 15$ GHz used by Rodríguez et al. (2003a) with two VLA observations at $\nu = 45$ GHz (from 1998 and 2006; they do not include all the 45 GHz observations reported by Villa et al. 2017). They analysed the results assuming a circular orbit inclined by 60° but oriented at the same position angle as the circumstellar discs (P.A. = 165°) rather than exactly in the north–south direction as did Rodríguez et al. (2003a) and Villa et al. (2017). Under these assumptions, their relative astrometry implies an orbital period $P \approx 377$ yr, a semimajor axis $a \approx 52.5$ au, and a total mass for the system of the order of $M_{\text{tot}} \approx 1.0 M_\odot$.¹ Lim & Takakuwa (2006) and, more recently, Lim et al. (2016) also discuss the possibility of elliptic orbits. In addition to the astrometry, and following Pichardo, Sparke & Aguilar (2005), they incorporate dynamical constraints imposed by the outer radii of the circumstellar discs and the inner radius of the circumbinary disc. They conclude that orbits with modest eccentricities ($e \lesssim 0.3$) are favoured.

A full astrometric study of L 1551 IRS 5 that includes all the existing high resolution VLA observations, is still missing. In addition, ALMA has now observed this system several times with sufficient angular resolution to contribute to the monitoring of its astrometry (Cruz-Sáenz de Miera et al. 2019; Bianchi et al. 2020; Takakuwa et al. 2020). Finally, only two studies (Rodríguez et al. 2003a; Villa et al. 2017) have, so far, considered the absolute proper motion of L 1551 IRS 5 and they arrive at somewhat uncertain and incompatible results. In this paper, we combine all existing suitable observations of L 1551 IRS 5 obtained with the VLA and ALMA interferometers to revisit both the relative and the absolute astrometry of the system. While the previous studies were based on a scant handful of observations, ours incorporate over 30 individual observations, spanning nearly 40 yr. The data are described in Section 2. The resulting absolute and relative proper motions are presented in Section 3 and discussed in Section 4. Finally, in Section 5 we present our conclusions and discuss future perspectives for the study of L 1551 IRS 5 and other systems.

2 OBSERVATIONS AND DATA PROCESSING

2.1 Data selection and calibration

We searched the VLA and ALMA data archives for observations of L 1551 IRS 5 with sufficient angular resolution to resolve the two sources in the system. Since they are separated by about $0''.33$, we selected only those data with an angular resolution better than about $0''.3$. In the case of the VLA, this implies considering only observations at frequencies higher than 10 GHz – i.e. in bands X (~ 10 GHz), Ku (~ 15 GHz), K (~ 22 GHz), Ka (~ 33 GHz), and Q (~ 45 GHz). It also restricts us to the most extended configuration (A) of the array for bands X and Ku, and the two most extended configurations (A and B) for bands K, Ka, and Q. We found 30 individual observations matching these requirements in the VLA archive. They span the time range from 1983 to 2022; 22 of these observations were obtained before the VLA upgrade (Perley et al. 2011), while the other eight were collected after the upgrade. We will distinguish between these two subsets of VLA observations in the rest of the paper by referring to them as *historical* VLA and *Jansky* VLA observations, respectively. The data sets considered here include the four observations at $\nu = 15$ GHz reported by Rodríguez et al. (2003a) and Lim & Takakuwa (2006), as well as the 45 GHz

¹For consistency with the figures reported in this paper, the values of the semimajor axis and mass have been re-scaled to a distance of 146.4 pc, from their original values calculated assuming $d = 140$ pc.

Table 1. List of VLA and ALMA observations of L 1551 IRS 5.

Index	Date	Band	Gain calibrator (J2000)	Project (segment)	Beam size (arcsec × arcsec; °)	Noise (mJy)	Robust
1	1983.89	Ku	0403 + 260	AC0089 (A,B)	0.13×0.12; −25.63	0.08	0.5
2	1984.90	Ku	0403 + 260	AS0206 (C)	0.15×0.13; −34.61	0.14	2.0
3	1985.01	Ku	0503 + 012	AR0121 (A)	0.12×0.12; −22.89	0.09	0.5
4	1987.60	Ku	0409 + 122	AC0188 (A,B)	0.13×0.13; +60.69	0.04	0.5
5	1988.88	Ku	0409 + 122	AC0241 (A)	0.14×0.13; +86.77	0.05	0.5
6	1994.31	X	0403 + 260	AR0277 (A,C)	0.17×0.16; −89.21	0.02	−2.0
7	1994.32	Ku	0403 + 260	AR0277 (A,D)	0.14×0.11; +89.17	0.06	2.0
8	1995.57	X	0403 + 260	AC0435 (A)	0.18×0.16; −7.34	0.02	−2.0
9	1995.57	Ku	0403 + 260	AC0435 (A)	0.17×0.15; −16.18	0.06	2.0
10	1995.79	K	0510 + 180	AK0418 (A,B)	0.27×0.23; −10.97	0.20	2.0
11	1996.94	X	0510 + 180	AR0277 (G,H)	0.18×0.16; −04.69	0.02	−2.0
12	1996.94	Ku	0510 + 180	AR0277 (G,H)	0.13×0.12; +17.37	0.06	0.5
13	1997.03	Q	0431 + 206	AR0277 (N)	0.10×0.05; −31.66	0.16	2.0
14	1998.41	X	0403 + 260	AC0502 (A)	0.18×0.17; −07.75	0.02	−2.0
15	1998.41	Ku	0403 + 260	AC0502 (A)	0.15×0.12; −66.87	0.07	0.5
16	2000.00	Q	0431 + 206	AT0235 (A,B)	0.18×0.14; −40.16	0.20	2.0
17	2002.09	Q	0431 + 175	AT0269 (A,B)	0.06×0.04; −23.36	0.06	2.0
18	2002.15	X	0510 + 180	AR0475 (A)	0.16×0.16; −75.89	0.01	−2.0
19	2003.60	X	0510 + 180	AR0516 (B)	0.18×0.17; +02.48	0.02	−0.5
20	2003.68	Q	0431 + 206	AC0675 (A)	0.06×0.05; −18.98	0.12	2.0
21	2003.83	Q	0431 + 175	AL0606 (A,B)	0.17×0.15; −12.89	0.05	2.0
22	2004.89	Q	0431 + 175	AC0743 (A)	0.05×0.05; +03.69	0.07	2.0
23	2012.90	Q	0431 + 175	12B-091 (X ₁ ,X ₂ ,X ₃)	0.06×0.05; +14.73	0.01	2.0
24	2013.95	Q	0431 + 175	13B-122 (X ₁ ,X ₂ ,X ₃ ,X ₄)	0.17×0.17; −18.99	0.01	2.0
25	2017.56	6	0510 + 180	2016.1.00209.S	0.14×0.10; +88.83	0.42	−2.0
26	2017.57	7	0431 + 175	2016.1.00138.S	0.08×0.06; +71.70	0.32	−2.0
27	2017.84	4	0431 + 206	2017.1.00388.S	0.06×0.04; −33.05	0.09	0.0
28	2017.88	3	0431 + 206	2017.1.00388.S	0.12×0.09; +18.72	0.05	0.0
29	2018.82	6	0510 + 180	2018.1.01205.L	0.20×0.20; +40.76	0.6	−2.0
30	2019.48	Ka	0431 + 175	18B-179 (X ₆ ,X ₁₄)	0.30×0.15; −58.24	0.03	0.5
31	2020.97	X	0449 + 113	20B-345 (X ₁)	0.14×0.13; +10.78	0.02	−2.0
32	2020.99	K	0431 + 206	20B-122 (X ₁)	0.07×0.06; −32.76	0.02	−0.5
33	2021.02	Ku	0431 + 206	20B-122 (X ₂)	0.11×0.09; −63.09	0.008	−0.5
34	2021.04	X	0431 + 206	20B-122 (X ₃)	0.16×0.15; +38.99	0.02	−1.5
35	2021.63	6	0431 + 175	2019.1.01074.S	0.05×0.04; −14.14	0.08	0.5
36	2021.69	3	0431 + 175	2019.1.01074.S	0.07×0.04; −32.39	0.02	0.5
37	2022.32	X	0449 + 113	22A-065 (X ₁ ,X ₂)	0.18×0.14; +63.03	0.007	−0.5

Note. For some projects (e.g. AC0089 or AC0188), several segments were observed on slightly different dates. In such cases, while the data were calibrated separately, the images combined the visibilities from the various segments. The sources are not expected to move appreciably during the short separations (from a few days to a few weeks) between the segments.

observations reported by Villa et al. (2017), Lim & Takakuwa (2006), and Lim et al. (2016). In the ALMA archive, we identified a total of seven observations with sufficient angular resolution to resolve the L 1551 IRS 5 system; they were obtained in bands 3 (~100 GHz), 4 (~150 GHz), 6 (~230 GHz), and 7 (~330 GHz) between 2017 and 2021. The complete list of observations considered here is given in Table 1; it spans 38.4 years from late 1983 to early 2022.

The historical VLA observations simultaneously recorded both circular polarization components (R and L) and an effective bandwidth of 100 MHz (2×50 MHz). In a few instances, the Pie Town Very Long Baseline Array antenna (Napier et al. 1994) was used together with the VLA as a way of increasing the angular resolution. In such cases, we discarded the Pie Town antenna from our analysis because (i) the data without Pie Town had sufficient angular resolution to resolve L 1551 IRS 5, and (ii) including Pie Town results in a highly inhomogeneous (u, v) coverage that complicates the imaging process. The calibration was performed in CASA (Common Astronomy Software Applications, McMullin et al. 2007; The CASA Team 2022) version 5.7.0 following standard procedures. First, the

data were inspected and bad visibilities were flagged. Secondly, amplitudes and phase corrections were determined using observations of a nearby gain calibrator (listed in column 4 of Table 1). Lastly, the absolute flux density was established using observations of a standard flux calibrator. No self-calibration was attempted given the modest signal-to-noise level of the resulting images.

The Jansky VLA observations (projects 12B-091, 13B-122, 20B-345, 18B-179, and 22A-065) also recorded the two components of circular polarization, but with a much wider bandwidth (8 GHz in bands K, Ka, and Q; 6 GHz in band Ku, and 4 GHz in band X). The data were calibrated using the dedicated VLA Pipeline (version 2022.2.0.64) distributed as part of the CASA software (version 6.4.1). The pipeline implements the same steps as discussed in the previous paragraph for the historical VLA data (including some flagging), as well as additional steps – for instance, bandpass calibration which becomes necessary because of the increased bandwidth. Inspection of the diagnostic plots produced by the pipeline led us to implement some additional flagging before proceeding to the imaging steps. Given the high signal-to-noise ratio in the resulting images, self-

calibration was possible and resulted in a significant improvement in the final image noise levels. We verified that self-calibration did not affect the astrometry by comparing the positions in the images obtained with and without self-calibration. Since self-calibration improves the image quality but not the quality of the astrometry, we used the astrometric errors from the images *before* self-calibration. The UV-data corresponding to the project 20B-122 were provided by the project principal investigators; calibration details for this project data are described by Feeney-Johansson et al. (2023).

In this work, we focused primarily on the northern and southern protostars in the L1551 IRS 5 system. We have also monitored two additional components that appear near the northern source and the southern source, respectively (see Section 2.2 below) in centimetric observations (X, Ku, and K bands). Appendix A includes the full set of VLA images that were considered in this work and shows the weighting used for each image. As a general rule, in those observations where we were able to clearly resolve all the objects of interest, the calibrated visibilities were imaged using natural weighting (ROBUST = 2) to optimize the signal-to-noise level. On the other hand, when we could not resolve the different components using natural weighting, a different weighting scheme was used (different for each image; see Appendix A).

The ALMA data were calibrated and provided by the principal investigator of each project.² The continuum images corresponding to projects 2016.1.00209.S and 2016.1.00138.S were published by Cruz-Sáenz de Miera et al. (2019) and Takakuwa et al. (2020), respectively, and the details of the calibration, as well as the images, can be consulted there. Specifically for project 2016.1.00209.S, we use an image obtained from only the long baseline configuration that emphasizes the compact sources against the more extended emission. The images in bands 3 and 4 corresponding to project 2017.1.00388.S were obtained from the NRAO data base. Project 2018.1.01205.L is a large ALMA project called FAUST (Codella et al. 2021). Part of the L 1551 IRS 5 data have been published by Bianchi et al. (2020) where the calibration steps are described, but the image we use here was again obtained by using only the extended baseline configuration. The observations corresponding to project 2019.1.01074.S will be published in a forthcoming paper by M.J. Maureira and collaborators.

2.2 Source positions and astrometric corrections

In most higher frequency VLA images (bands Q, Ka, and K), only two compact sources (associated with L 1551 IRS 5 N and S; crosses in the images shown in Appendix A) are detected. At lower VLA frequencies (bands Ku and X), we often see additional peaks, presumably associated with shock features – their detection only at lower frequency indicates optically thin free–free emission or possibly emission of non-thermal nature such as synchrotron (Anglada, Rodríguez & Carrasco-González 2018). Indeed, these sources have fluxes of a few tenths of mJy, which is only a few times the noise level of the higher frequency VLA images obtained before the upgrade. One of these peaks is located to the north-east of L 1551 IRS 5 N. We will refer to this component as Sh-N (for Shock-North). The other peak is located to the north-east of L 1551 IRS 5 S, and will be called Sh-S (Sh-N and Sh-S are also indicated as crosses in Appendix A). In the Ku image corresponding to project AC0502, the emission associated with Sh-S presents a complicated morphology;

we will not take this image into account for the astrometry of Sh-S below. In several X band images, compact emission associated with L 1551 IRS 5 S is detected, but it is not resolved from the emission from Sh-S. The existence of Sh-N and Sh-S, as well as the varying morphology of L 1551 IRS 5 S at low frequencies almost certainly reflect ongoing jet activity. We will discuss this issue and its effect on astrometry extensively in Section 3.

For all epochs, we measured the positions of each source by fitting 2D Gaussian functions to the images (task IMFIT in CASA); these positions are reported in Table 2, columns 4 and 5. The task IMFIT provides errors on the source positions, but these errors greatly underestimate the true astrometric errors because it only accounts for Gaussian thermal noise on the visibility phases (Condon 1997). In reality, many other sources of uncertainty contribute to the astrometric error budget in interferometric observations (Reid & Honma 2014). In addition, *astrophysical noise* can be important if the source structure is variable or if different processes are at work at different frequencies. Feeney-Johansson et al. (2023) recently demonstrated the relevance of both points to the specific case of L 1551 IRS 5; in their detailed multi-epoch, multifrequency study of this source, they showed that the radio emission of both components of the system is a mix of thermal dust and free–free radiation and they documented significant morphological changes. We will come back to these issues momentarily, but we mention them here to justify why we do not report the errors provided by IMFIT in Table 2: in the case of L 1551 IRS 5, they are underestimated to the point of being irrelevant.

Before the measured positions can be used to study the astrometry of the system, two corrections must be applied. The first one is related to the gain calibrators used as astrometric references in interferometric observations and are of two (related) types. The catalogued positions of the calibrators used both at the VLA and ALMA have been refined over the years through dedicated observations. For instance, the positions of roughly half of the VLA calibrators was updated at the turn of the century thanks to new astrometric measurements obtained with the VLBA (Johnston et al. 1995; Beasley et al. 2002). As a consequence, even if a single gain calibrator has been used for all observations, its *catalogued* position may have changed significantly between observations. Indeed, we found that the catalogued position of the gain calibrator used in project AR0121 differs from its value in more recent observations by more than 140 mas. Similarly, for the Q band projects AR0277 and AT0235, the catalogued gain calibrator position is offset from its most recent value by about 90 mas. We will see in Section 3 and Appendix B that such large errors can strongly affect proper motion measurements. A related issue occurs when observations that use different gain calibrators are combined. This is relevant here since the observations were obtained using seven distinct calibrators (Table 1). In such cases, the astrometric error relevant for proper motion measurements is the quadratic combination of the errors affecting the catalogued positions of the various calibrators. The current VLA calibrator catalogue includes a code for each source which quantifies its astrometric error. The astrometric code of six of our calibrators is A, indicating a residual error smaller than 2 mas, while it is B (astrometric uncertainty between 2 and 10 mas) for the last one (0431+206). Thus, using the latest positions for all calibrators ought to ensure that the contribution of calibrator position uncertainty to the overall error budget is well below 10 mas. To first order, an error in the catalogued position of a calibrator results in a simple translation of the target position. If (α_0^c, δ_0^c) is the most recent position of a calibrator, (α_u^c, δ_u^c) the catalogued position used at a given epoch, and (α_m^t, δ_m^t) the measured position of the target at that

²The principal and some co-investigators of most ALMA projects used here are authors of this article.

Table 2. Positions of the sources in L 1551 IRS 5 before any astrometric correction, after the gain calibrator catalogued position correction, and after the gain calibrator catalogued position correction and the parallax correction. The errors quoted in the last two columns include systematic errors derived from the fits (see the text). The data are shown in alternating normal and bold rows entries to facilitate the reading.

Date	Band	Component	Before any corrections		After gain calibrator correction		After parallax correction	
			R.A. (J2000) <i>s</i> from 04 ^h 31 ^m	Dec. (J2000) " from 18°08'	R.A. (J2000) <i>s</i> from 04 ^h 31 ^m	Dec. (J2000) " from 18°08'	R.A. (J2000) <i>s</i> from 04 ^h 31 ^m	Dec. (J2000) " from 18°08'
1983.89	Ku	North	34.1347	5.3454	34.1402	5.3344	34.1401 ± 0.0018	5.3346 ± 0.0250
		South	34.1305	5.0496	34.1360	5.0386	34.1359 ± 0.0018	5.0389 ± 0.0250
1984.90	Ku	North	34.1325	5.3043	34.1380	5.2933	34.1379±0.0018	5.2936±0.0250
		South	34.1269	5.0416	34.1324	5.0306	34.1323±0.0018	5.0309±0.0250
		Sh-S	34.1402	5.1432	34.1457	5.1322	34.1456±0.0015	5.1326±0.0211
1985.01	Ku	North	34.1381	5.1584	34.1370	5.3003	34.1373 ± 0.0018	5.3013 ± 0.0250
		Sh-N	34.1506	5.2367	34.1494	5.3787	34.1497 ± 0.0025	5.3797 ± 0.0300
		South	34.1351	4.8597	34.1339	5.0017	34.1342 ± 0.0018	5.0027 ± 0.0250
		Sh-S	34.1447	4.9610	34.1436	5.1030	34.1438 ± 0.0015	5.1039 ± 0.0211
1987.60	Ku	North	34.1400	5.1831	34.1409	5.2431	34.1405±0.0018	5.2420±0.0250
		South	34.1355	4.8661	34.1364	4.9261	34.1360±0.0018	4.9250±0.0250
		Sh-S	34.1441	4.9615	34.1450	5.0215	34.1446±0.0015	5.0204±0.0211
1988.88	Ku	North	34.1393	5.1524	34.1402	5.2124	34.1401 ± 0.0018	5.2126 ± 0.0250
		South	34.1377	4.8700	34.1386	4.9300	34.1385 ± 0.0018	4.9302 ± 0.0250
		Sh-S	34.1462	4.9329	34.1471	4.9929	34.1470 ± 0.0015	4.9930 ± 0.0211
1994.31	X	North	34.1454	5.1316	34.1450	5.1326	34.1453±0.0022	5.1329±0.0300
		Sh-N	34.1627	5.2349	34.1623	5.2359	34.1626±0.0025	5.2361±0.0300
		South + Sh-S	34.1479	4.8585	34.1475	4.8595	34.1478±0.0022	4.8598±0.0300
1994.32	Ku	North	34.1454	5.1213	34.1450	5.1223	34.1452 ± 0.0018	5.1225 ± 0.0250
		Sh-N	34.1596	5.2643	34.1592	5.2653	34.1595 ± 0.0025	5.2655 ± 0.0300
		South	34.1416	4.7863	34.1413	4.7873	34.1415 ± 0.0018	4.7875 ± 0.0250
		Sh-S	34.1490	4.8874	34.1487	4.8884	34.1489 ± 0.0015	4.8886 ± 0.0211
1995.57	X	North	34.1487	5.0987	34.1484	5.0997	34.1480±0.0022	5.0986±0.0302
		South	34.1464	4.7916	34.1461	4.7926	34.1457±0.0022	4.7915±0.0300
		Sh-S	34.1550	4.8743	34.1546	4.8753	34.1542±0.0015	4.8742±0.0211
1995.57	Ku	North	34.1461	5.0821	34.1457	5.0831	34.1453 ± 0.0018	5.0820 ± 0.0250
		South	34.1438	4.7605	34.1434	4.7615	34.1430 ± 0.0018	4.7604 ± 0.0250
		Sh-S	34.1555	4.9025	34.1551	4.9035	34.1547 ± 0.0015	4.9025 ± 0.0211
1995.79	K	North	34.1447	5.1125	34.1447	5.1125	34.1444±0.0007	5.1121±0.0102
		South	34.1436	4.7790	34.1436	4.7790	34.1433±0.0007	4.7786±0.0100
1996.94	X	North	34.1456	5.0645	34.1456	5.0645	34.1456 ± 0.0022	5.0651 ± 0.0300
		Sh-N	34.1586	5.1400	34.1586	5.1400	34.1587 ± 0.0025	5.1406 ± 0.0300
		South	34.1434	4.7354	34.1434	4.7354	34.1435 ± 0.0022	4.7360 ± 0.0300
		Sh-S	34.1522	4.8275	34.1522	4.8275	34.1522 ± 0.0015	4.8281 ± 0.0211
1996.94	Ku	North	34.1463	5.0641	34.1463	5.0641	34.1463±0.0018	5.0647±0.0250
		South	34.1431	4.7412	34.1431	4.7412	34.1432±0.0018	4.7418±0.0250
		Sh-S	34.1513	4.8022	34.1513	4.8022	34.1514±0.0015	4.8029±0.0211
1997.03	Q	North	34.1403	5.0548	34.1466	5.0535	34.1469 ± 0.0007	5.0545 ± 0.0101
		South	34.1396	4.7233	34.1459	4.7221	34.1463 ± 0.0007	4.7231 ± 0.0101
1998.41	X	North	34.1460	5.0604	34.1460	5.0604	34.1460±0.0022	5.0600±0.0300
		Sh-N	34.1660	5.1884	34.1660	5.1884	34.1660±0.0025	5.1879±0.0300
		South + Sh-S	34.1515	4.7961	34.1515	4.7961	34.1516±0.0022	4.7957±0.0300
1998.41	Ku	North	34.1483	5.0652	34.1483	5.0652	34.1483 ± 0.0018	5.0647 ± 0.0250
		Sh-N	34.1619	5.1453	34.1619	5.1453	34.1619 ± 0.0025	5.1448 ± 0.0300
		South	34.1464	4.7462	34.1464	4.7462	34.1464 ± 0.0018	4.7458 ± 0.0250
2000.00	Q	North	34.1428	5.0009	34.1491	4.9989	34.1493±0.0007	4.9998±0.0100
		South	34.1424	4.6742	34.1487	4.6722	34.1489±0.0007	4.6731±0.0100
2002.09	Q	North	34.1492	4.9745	34.1493	4.9749	34.1497 ± 0.0007	4.9760 ± 0.0102
		South	34.1496	4.6447	34.1496	4.6451	34.1500 ± 0.0007	4.6462 ± 0.0101
2002.15	X	North	34.1488	4.9741	34.1488	4.9738	34.1493±0.0022	4.9749±0.0300
		Sh-N	34.1662	5.0721	34.1662	5.0718	34.1667±0.0025	5.0728 ± 0.0300
		South + Sh-S	34.1563	4.7209	34.1563	4.7206	34.1568±0.0022	4.7216±0.0300
2003.60	X	North	34.1517	4.9346	34.1517	4.9353	34.1513 ± 0.0022	4.9341 ± 0.0300
		Sh-N	34.1635	5.0657	34.1635	5.0664	34.1631 ± 0.0025	5.0653 ± 0.0300
		South	34.1498	4.5626	34.1498	4.5633	34.1493 ± 0.0022	4.5622 ± 0.0300
		Sh-S	34.1602	4.7162	34.1602	4.7169	34.1598 ± 0.0015	4.7158 ± 0.0211
2003.68	Q	North	34.1527	4.9397	34.1527	4.9394	34.1522±0.0007	4.9383±0.0100
		South	34.1529	4.6074	34.1529	4.6071	34.1524±0.0007	4.6061±0.0100
2003.83	Q	North	34.1516	4.9483	34.1516	4.9487	34.1514 ± 0.0007	4.9486 ± 0.0100
		South	34.1523	4.6147	34.1523	4.6151	34.1521 ± 0.0007	4.6149 ± 0.0100
2004.89	Q	North	34.1517	4.9328	34.1519	4.9332	34.1519±0.0007	4.9334±0.0100

Table 2 – continued

Date	Band	Component	Before any corrections		After gain calibrator correction		After parallax correction	
			R.A. (J2000) ^s from 04 ^h 31 ^m	Dec. (J2000) " from 18°08'	R.A. (J2000) ^s from 04 ^h 31 ^m	Dec. (J2000) " from 18°08'	R.A. (J2000) ^s from 04 ^h 31 ^m	Dec. (J2000) " from 18°08'
2012.90	Q	South	34.1523	4.5921	34.1525	4.5925	34.1525±0.0007	4.5928±0.0100
		North	34.1575	4.7933	34.1576	4.7928	34.1575 ± 0.0007	4.7931 ± 0.0100
2013.95	Q	South	34.1601	4.4379	34.1601	4.4373	34.1601±0.0007	4.4376±0.0100
		North	34.1585	4.7701	34.1586	4.7695	34.1587±0.0007	4.7701±0.0100
2017.56	6	South	34.1614	4.4168	34.1614	4.4162	34.1615±0.0007	4.4168±0.0100
		North	34.1624	4.7168	34.1625	4.7165	34.1621 ± 0.0009	4.7154 ± 0.0080
2017.57	7	South	34.1663	4.3610	34.1664	4.3607	34.1660±0.0009	4.3596±0.0080
		North	34.1610	4.7220	34.1610	4.7219	34.1606±0.0009	4.7208±0.0081
2017.84	4	South	34.1650	4.3590	34.1650	4.3589	34.1646±0.0009	4.3578±0.0081
		North	34.1609	4.6957	34.1609	4.6957	34.1607 ± 0.0009	4.6956 ± 0.0080
2017.89	3	South	34.1648	4.3370	34.1648	4.3370	34.1646±0.0009	4.3369±0.0080
		North	34.1614	4.7030	34.1614	4.7030	34.1613±0.0009	4.7032±0.0080
2018.82	6	South	34.1652	4.3428	34.1652	4.3428	34.1651±0.0009	4.3430±0.0080
		North	34.1634	4.6816	34.1634	4.6816	34.1631 ± 0.0009	4.6813 ± 0.0081
2019.48	Ka	South	34.1672	4.3163	34.1672	4.3163	34.1669±0.0009	4.3160±0.0081
		North	34.1640	4.6730	34.1640	4.67240	34.1639 ± 0.0007	4.6716±0.0100
2020.97	X	South	34.1674	4.3103	34.1674	4.3097	34.1672±0.0007	4.3089±0.0100
		North	34.1632	4.6358	34.1643	4.6354	34.1645 ± 0.0022	4.6361 ± 0.0300
2020.99	K	South	34.1655	4.2753	34.1667	4.2749	34.1668±0.0022	4.2756±0.0300
		Sh-S	34.1736	4.3418	34.1747	4.3415	34.1749 ± 0.0015	4.3422 ± 0.0211
2021.02	Ku	South	34.1631	4.6323	34.1631	4.6323	34.1633±0.0007	4.6332±0.0100
		Sh-S	34.1671	4.2670	34.1671	4.2670	34.1673±0.0007	4.2678±0.0100
2021.04	X	South	34.1740	4.3335	34.1740	4.3335	34.1742±0.0015	4.3344±0.0211
		North	34.1633	4.6262	34.1633	4.6262	34.1636 ± 0.0018	4.6272 ± 0.0250
2021.63	6	South	34.1676	4.2587	34.1676	4.2587	34.1679±0.0018	4.2596±0.0250
		Sh-S	34.1740	4.3226	34.1740	4.3226	34.1743 ± 0.0015	4.3236 ± 0.0211
2021.69	3	South	34.1619	4.6215	34.1619	4.6215	34.1622±0.0022	4.6226±0.0300
		South + Sh-S	34.1725	4.3207	34.1725	4.3207	34.1729±0.0022	4.3217±0.0300
2022.32	X	South	34.1636	4.6332	34.1636	4.6331	34.1632±0.0009	4.6320±0.0082
		North	34.1683	4.2683	34.1684	4.2682	34.1679 ± 0.0009	4.2671 ± 0.0081
2022.32	X	South	34.1641	4.6344	34.1641	4.6343	34.1636±0.0009	4.6334±0.0081
		North	34.1687	4.2695	34.1687	4.2695	34.1682±0.0009	4.2685±0.0080
2022.32	X	South	34.1632	4.6284	34.1634	4.6280	34.1636±0.0022	4.6282±0.0300
		Sh-N	34.1823	4.7567	34.1824	4.7563	34.1827 ± 0.0025	4.7565 ± 0.0300
		South + Sh-S	34.1712	4.2973	34.1713	4.2969	34.1716 ± 0.0022	4.2971 ± 0.0300

epoch, then the corrected position of the target (α_c^t, δ_c^t) is:

$$\alpha_c^t = \alpha_m^t + (\alpha_0^c - \alpha_u^c) \frac{\cos \delta^c}{\cos \delta^t} \quad \text{and} \quad \delta_c^t = \delta_m^t + (\delta_0^c - \delta_u^c), \quad (1)$$

where $\delta^c = \frac{1}{2}(\delta_0^c + \delta_u^c)$ and $\delta^t = \frac{1}{2}(\delta_m^t + \delta_c^t)$ are used for the declinations of the calibrator and target in the small angle approximation for the shifts in right ascension. The positions of the sources in L 1551 IRS 5 after applying these calibrator position corrections are listed in columns 6 and 7 of Table 2.

The second correction that must be applied to the positions before using them for proper motion measurements accounts for the trigonometric parallax of the source, which produces an elliptical apparent displacement of the target on the celestial sphere. The trigonometric parallax of the L 1551 dark cloud is $\varpi = 6.83 \pm 0.03$ mas (Galli et al. 2018) so the semimajor axis of the parallactic ellipse is about 13 mas. We shall see in Section 3 that, although small, this effect is not negligible compared with our measurement errors. For a source in the direction (α, δ), the projection of the unit trigonometric parallax ellipse along right ascension and declination are:

$$f_\alpha = \frac{1}{\cos \delta} (X \sin \alpha - Y \cos \alpha) \quad (2)$$

$$f_\delta = X \cos \alpha \sin \delta + Y \sin \alpha \sin \delta - Z \cos \delta, \quad (3)$$

where (X, Y, Z) are the barycentric coordinates of the Earth at the time of the observations (Seidemann 1992); they were calculated using the NOVAS package (Barron et al. 2011). The positions corrected for the effect of parallax (α_c, δ_c) are obtained from the measured coordinates (α_m, δ_m) using:

$$\alpha_c = \alpha_m - \varpi f_\alpha \quad \text{and} \quad \delta_c = \delta_m - \varpi f_\delta. \quad (4)$$

The positions of the sources in L 1551 IRS 5 after applying these corrections (as well as the calibrator position corrections discussed earlier) are listed in columns 8 and 9 of Table 2.

From the measured coordinates, we calculated the relative position between the two protostars in L 1551 IRS 5. Here, we excluded all X band observations as well as some of the Ku band data where the astrometry of L 1551 IRS 5 S is affected by the presence of Sh-S. Such an effect had already been noticed by Rodríguez et al. (2003a). Following Rodríguez et al. (2003a), Villa et al. (2017), and Lim & Takakuwa (2006), the relative positions are defined with respect to the northern source:

$$\Delta\alpha = 15(\alpha_S - \alpha_N) \cos \delta \quad \text{and} \quad \Delta\delta = \delta_S - \delta_N. \quad (5)$$

We also express the relative positions between the sources in terms of their separation and position angle (ρ, θ) defined in a standard

Table 3. Relative positions of L 1551 IRS 5 N and S.

Date	Band	$\Delta\alpha$ (mas)	$\Delta\delta$ (mas)	ρ (mas)	θ (°)
1983.89	Ku	-59 ± 18	-296 ± 18	302 ± 18	191 ± 3
1985.01	Ku	-44 ± 18	-299 ± 18	302 ± 18	188 ± 3
1994.32	Ku	-53 ± 18	-335 ± 18	339 ± 18	189 ± 3
1995.57	Ku	-33 ± 18	-322 ± 18	323 ± 18	186 ± 3
1995.79	K	-16 ± 5	-333 ± 5	334 ± 5	183 ± 1
1996.94	Ku	-45 ± 18	-323 ± 18	326 ± 18	188 ± 3
1997.03	Q	-9 ± 5	-331 ± 5	332 ± 5	181 ± 1
1998.41	Ku	-27 ± 18	-319 ± 18	320 ± 18	185 ± 3
2000.00	Q	-6 ± 5	-327 ± 5	327 ± 5	181 ± 1
2002.09	Q	$+5 \pm 5$	-330 ± 6	330 ± 6	179 ± 1
2003.68	Q	$+3 \pm 5$	-332 ± 5	332 ± 5	180 ± 1
2003.83	Q	$+10 \pm 5$	-334 ± 5	334 ± 5	178 ± 1
2004.89	Q	$+9 \pm 5$	-341 ± 5	341 ± 5	179 ± 1
2012.90	Q	$+36 \pm 5$	-355 ± 5	357 ± 5	174 ± 1
2013.95	Q	$+40 \pm 5$	-353 ± 5	356 ± 5	174 ± 1
2017.56	6	$+56 \pm 3$	-356 ± 3	360 ± 3	171 ± 1
2017.57	7	$+57 \pm 3$	-363 ± 3	367 ± 3	171 ± 1
2017.84	4	$+56 \pm 3$	-359 ± 3	363 ± 3	171 ± 1
2017.89	3	$+55 \pm 3$	-360 ± 3	364 ± 3	171 ± 1
2018.82	6	$+54 \pm 3$	-365 ± 3	369 ± 3	172 ± 1
2019.48	Ka	$+48 \pm 5$	-363 ± 5	366 ± 5	172 ± 1
2020.99	K	$+57 \pm 18$	-365 ± 5	370 ± 6	171 ± 3
2021.02	Ku	$+61 \pm 18$	-368 ± 18	372 ± 18	171 ± 3
2021.63	6	$+67 \pm 3$	-365 ± 4	371 ± 4	170 ± 1
2021.69	3	$+66 \pm 3$	-365 ± 3	371 ± 3	170 ± 1

Note. $\Delta\alpha$ and $\Delta\delta$ are the (equatorial) components of the offsets between L 1551 IRS 5 N and S; ρ is the separation between them, and θ is their relative position angle. The values correspond to the position of L 1551 IRS 5 S relative to N.

manner:

$$\rho = \sqrt{\Delta\alpha^2 + \Delta\delta^2} \quad \text{and} \quad \theta = 90^\circ - \arctan \frac{\Delta\delta}{\Delta\alpha}. \quad (6)$$

In the calculation of θ , care must be taken to extract the value of the arc-tangent adequate for each quadrant; this is effectively achieved by using the function `arctan2` of the `numpy` Python package. Note that the corrections mentioned earlier have no effect on the relative positions: the corrections are the same for all sources in the system so they cancel out when considering relative positions. The relative positions are listed in Table 3.

3 RESULTS

3.1 Absolute proper motions

The positions of L 1551 IRS 5 N and S as a function of time after all corrections are applied, are shown in Fig. 1 (in this first step, we exclude all X band data). It is clear that, to a good degree of approximation, both sources are moving uniformly along both axes of the equatorial system, so it is reasonable to fit the data points with a linear and uniform proper motion. In order to constrain the errors on the fitted parameters, however, it is necessary to specify the errors on the individual data points. As mentioned earlier, the errors provided by IMFIT strongly underestimate the true uncertainties. Fig. 1 clearly indicates that the dispersion on the Ku data points is larger than for the other bands. We found that adding quadratically 25 mas to the IMFIT errors in band Ku, 10 mas in all other VLA bands (K, Ka, and Q), and 8 mas in all ALMA bands (3, 4, 6, and 7) results in reduced χ^2 values of the order of 1 on the fits – both for the fits to all data points taken together, and for the fits to the Ku, Q, and ALMA bands

individually. We note that Rodríguez et al. (2003a) arrived at a similar conclusion, and quadratically added 20 mas to the measured errors on their Ku band observations. We argue that the dominant source of systematic errors in the case of Ku band is likely astrophysical. Indeed, as we will see momentarily, the low frequency images (bands Ku and X) of the southern source appear to be frequently affected by jet activity.

The fits to the data were performed using the Levenberg–Marquardt-based task `curve_fit` of the `scipy.optimize` Python package with a first-order polynomial function (i.e. a straight line). The results are provided in Table 4 and shown graphically in Fig. 1. To visually provide an indication of the uncertainties of the fits, Fig. 1 shows the best fit as a solid black line and, in cyan, 100 different realizations of the fit which sample (in a Monte Carlo sense) the possible values of the free parameters. For comparison with previously published results, we have also performed fits to the positions before the corrections were applied, and report the results in Table 4; the positions before applying the corrections are shown in Appendix B. The improvements resulting from the application of the corrections will be discussed momentarily and in Appendix B.

We now proceed to consider all data, including the X-band observations. In Fig. 2, we include the positions shown in Fig. 1 as black symbols. Additionally, orange symbols show the positions of L 1551 IRS 5 N and S (circles) and Sh-N and S (diamonds) in the X-band observations. From this figure, it is clear that Sh-N and Sh-S follow trajectories roughly parallel to L 1551 IRS 5 N and S, respectively. Armed with this knowledge, we can refine the determination of the proper motions of L 1551 IRS 5 N and S by repeating the fits including all observations that trace each protostar. These refined results are given in the last row of Table 4 and shown graphically in Fig. 2. They are fully consistent with, and slightly more accurate than, the initial values reported earlier. As can be seen in Table 4, the quality of the fits, as measured by the value of the χ^2 , improves significantly after the corrections for gain calibrator positions are applied. This is largely due to a few older epochs that used catalogued positions differing from their current values by tens of mas. The improvement after applying the parallax corrections is significantly smaller but still measurable – all values of χ^2 decrease after that correction is applied. After the corrections are applied, the proper motions of L 1551 IRS 5 N and S are determined to an accuracy of the order of 0.2 mas yr^{-1} . This is about one order of magnitude better than previous determinations (Table 4). Our results are compatible, within one sigma, with those reported by Rodríguez et al. (2003a) and Villa et al. (2017) for their subgroup 2. They are not consistent, however, with the proper motions reported by Villa et al. (2017) for their subgroup 1 or their entire sample.³ As shown in Appendix B, this discrepancy is due to the fact that Villa et al. (2017) did not correct for changes over time in the catalogued position of one of the gain calibrators.

To complete the study of proper motions in L 1551 IRS 5, we have measured the proper motions of Sh-N and Sh-S obtaining, respectively,

$$\mu_\alpha \cos \delta = +12.03 \pm 1.28 \text{ mas yr}^{-1} \quad (\text{Sh} - \text{N}) \quad (7)$$

$$\mu_\delta = -17.07 \pm 0.94 \text{ mas yr}^{-1} \quad (\text{Sh} - \text{N}) \quad (8)$$

with a reduced χ^2 of 1.46, and 0.78 for right ascension and

³As a reminder, subgroups 1 and 2 use different gain calibrators.

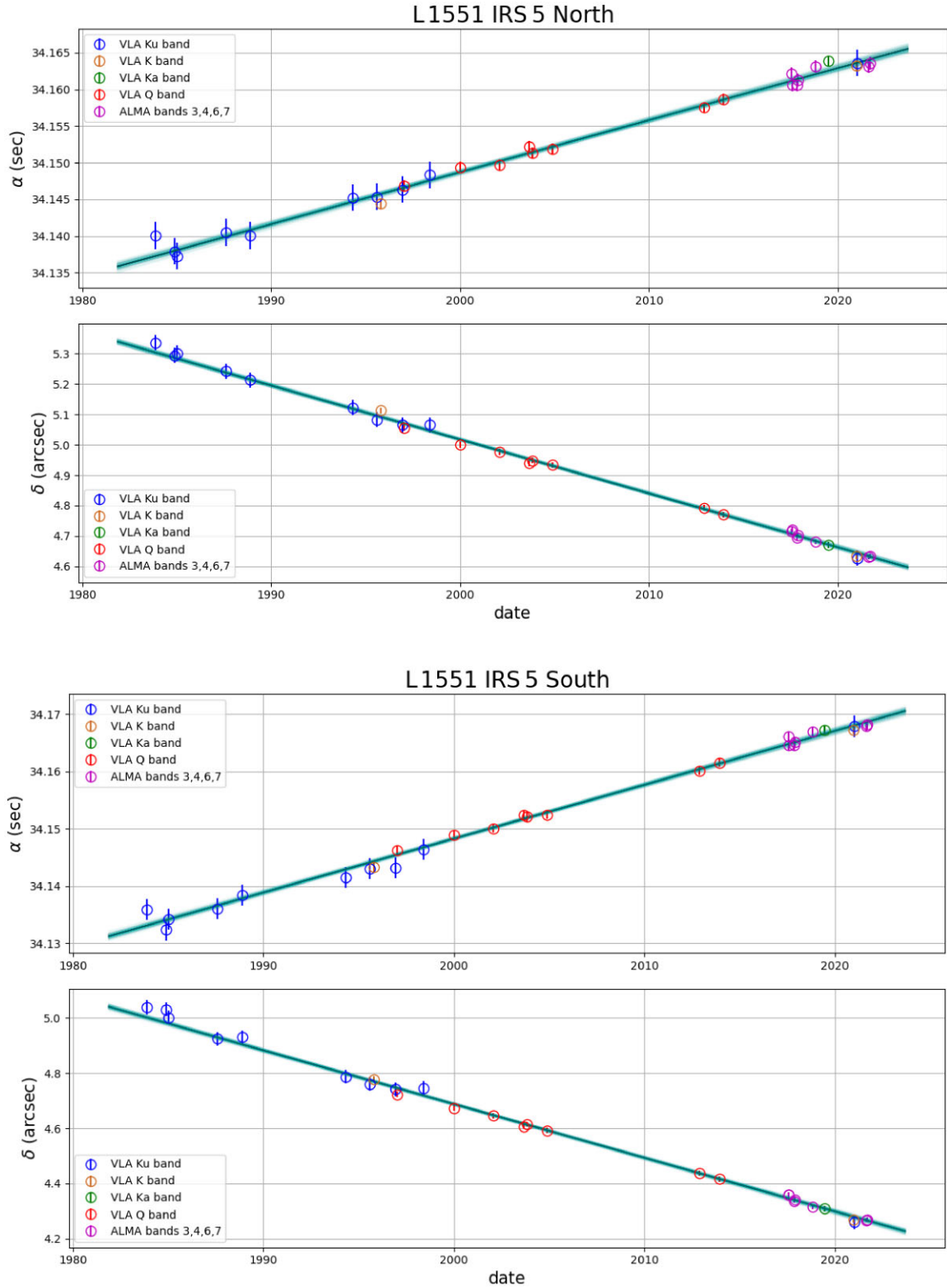


Figure 1. Position as a function of time of L 1551 IRS 5 N (top) and L 1551 IRS 5 S (bottom) after applying all astrometric corrections (gain calibrator positions and trigonometric parallax) in observations where the southern source is compact and single-peaked. The symbol colours indicate the different observing bands as given in the legends. The black straight line shows the best fit with a linear and uniform proper motion, and the semi-transparent cyan lines show 100 different realizations of the fit which sample (in a Monte Carlo sense) the possible values of the free parameters.

Table 4. Absolute proper motions of L 1551 IRS 5 N and S. The first four rows indicate measurements from the literature (see the text). The following three rows present our initial determinations before and after astrometric corrections are applied. The last row, shown in bold, contains our final proper motion determinations (see the text).

	L 1551 IRS 5N				L 1551 IRS 5S			
	$\mu_\alpha \cos \delta$ (mas yr ⁻¹)	χ_α^2 (N)	μ_δ (mas yr ⁻¹)	χ_δ^2 (N)	$\{\mu_\alpha \cos \delta$ (mas yr ⁻¹)	χ_α^2 (S)	μ_δ (mas yr ⁻¹)	χ_δ^2 (S)
	Previous works							
Rodríguez et al. (2003a)	11.7 ± 1.9		-20.3 ± 2.5		14.7 ± 1.6		-22.2 ± 2.8	
Villa et al. (2017) [Sub-group 1]	25.2 ± 1.0		-18.8 ± 2.0		30.0 ± 1.0		-20.6 ± 2.0	
Villa et al. (2017) [Sub-group 2]	10.8 ± 1.0		-16.9 ± 2.0		13.7 ± 1.0		-18.8 ± 2.0	
Villa et al. (2017)[Complete sample]	15.5 ± 3.7		-17.1 ± 0.8		19.2 ± 3.9		-19.2 ± 0.4	
	Present work (initial determination)							
No correction	11.56 ± 0.51	4.64	-17.29 ± 0.30	2.04	14.84 ± 0.49	4.31	-19.03 ± 0.30	2.07
Gain calibrator correction	10.23 ± 0.21	0.82	-17.70 ± 0.20	0.89	13.51 ± 0.21	0.81	-19.44 ± 0.22	1.05
Gain calibrator and parallax correction	10.12 ± 0.20	0.73	-17.73 ± 0.19	0.83	13.40 ± 0.20	0.72	-19.47 ± 0.21	0.99
	Present work (final determination)							
All epochs/corrections	10.10 ± 0.18	0.63	-17.75 ± 0.17	0.67	13.40 ± 0.20	0.72	-19.46 ± 0.21	0.99

Note. $\mu_\alpha \cos \delta$ and μ_δ are the components of the proper motions in right ascension and declination, respectively. The values of the χ^2 are indicated for each source/coordinate combination.

declination, respectively, and

$$\mu_\alpha \cos \delta = +12.14 \pm 0.36 \text{ mas yr}^{-1} \quad (\text{Sh} - \text{S}) \quad (9)$$

$$\mu_\delta = -21.16 \pm 0.35 \text{ mas yr}^{-1} \quad (\text{Sh} - \text{S}) \quad (10)$$

with reduced χ^2 of 0.71 in right ascension and 0.69 in declination.

Finally, we estimate the proper motions of L 1551 IRS 5 N and S including a quadratic term in the fits, in order to determine if acceleration has an important influence on the motions that we have observed so far. We obtained for L 1551 IRS 5 N

$$\mu_\alpha \cos \delta = +10.06 \pm 1.25 \text{ mas yr}^{-1} \quad (11)$$

$$\mu_\delta = -17.99 \pm 0.24 \text{ mas yr}^{-1} \quad (12)$$

$$a_\alpha \cos \delta = -0.01 \pm 0.11 \text{ mas yr}^{-2} \quad (13)$$

$$a_\delta = -0.07 \pm 0.07 \text{ mas yr}^{-2}, \quad (14)$$

where $a_\alpha \cos \delta$ and $a_\delta \cos \delta$ correspond to acceleration component for right ascension and declination, respectively. Similarly, for L 1551 IRS 5 S the results are

$$\mu_\alpha \cos \delta = +13.46 \pm 26 \text{ mas yr}^{-1} \quad (15)$$

$$\mu_\delta = -19.89 \pm 0.28 \text{ mas yr}^{-1} \quad (16)$$

$$a_\alpha \cos \delta = -0.03 \pm 0.10 \text{ mas yr}^{-2} \quad (17)$$

$$a_\delta = -0.03 \pm 0.07 \text{ mas yr}^{-2}. \quad (18)$$

Clearly, the acceleration terms are not significant at the current level of accuracy. This implies, in particular, that the curvature due to the binarity of the system is not yet detectable in the proper motions, and that no constraints can currently be derived on the mass ratio of the binary – the relative curvature of the individual orbital paths, if they could be measured, would provide direct constraints on the mass ratio. We did not attempt accelerated fits for the shock features Sh-N and Sh-S because the number of data points is limited and their dispersion is large.

3.2 Relative proper motions

The relative positions between L 1551 IRS 5 N and S (South relative to North) listed in Table 3 are shown graphically in Fig. 3 in two different forms: right ascension and declination offsets as a function of time, and separation and position angle as a function of time. Fits with linear and uniform proper motions along each variable were obtained using the same routines as in Section 3.1. The errors on the relative positions were estimated, as for the absolute positions, by requiring a reduced χ^2 of the order one for each band separately and for the overall fit. They happen to be slightly smaller (18 mas for band Ku, 5 mas for bands K, Ka and Q, and 3 mas for all ALMA bands) than the errors on the absolute positions. This is because any systematic instrumental error affects both sources equally and cancel out when the relative positions are calculated. The errors on the relative positions are, however, still significantly larger than the values derived from the IMFIT uncertainties. The best fit for ($\Delta\alpha$, $\Delta\delta$) as a function of time results in proper motions of:

$$\mu_{\Delta\alpha} = +3.29 \pm 0.11 \text{ mas yr}^{-1} \quad (19)$$

$$\mu_{\Delta\delta} = -1.60 \pm 0.09 \text{ mas yr}^{-1}. \quad (20)$$

We can verify the self-consistency of our results by comparing these values with the subtraction between the absolute proper motions of L 1551 IRS 5 N and S calculated in Section 3.1. The latter yields $\Delta\mu_\alpha = +3.30 \pm 0.27 \text{ mas yr}^{-1}$ and $\Delta\mu_\delta = -1.71 \pm 0.27 \text{ mas yr}^{-1}$. Clearly the two methods yield highly consistent results, but the fits to the relative positions result in a more accurate determination because, as mentioned earlier, the uncertainties on the relative positions are smaller than those on the absolute positions. For the separation and position angle between the sources, we obtain:

$$\mu_\rho = +1.82 \pm 0.09 \text{ mas yr}^{-1} \quad (21)$$

$$\mu_\theta = -0.52 \pm 0.02^\circ \text{ yr}^{-1}. \quad (22)$$

The fits are shown in Fig. 3 using the same representation as for the absolute proper motion fits: the black line shows the best fit, while the semitransparent cyan lines show 100 different realizations of the fit which sample the possible values of the free parameters. It is perhaps

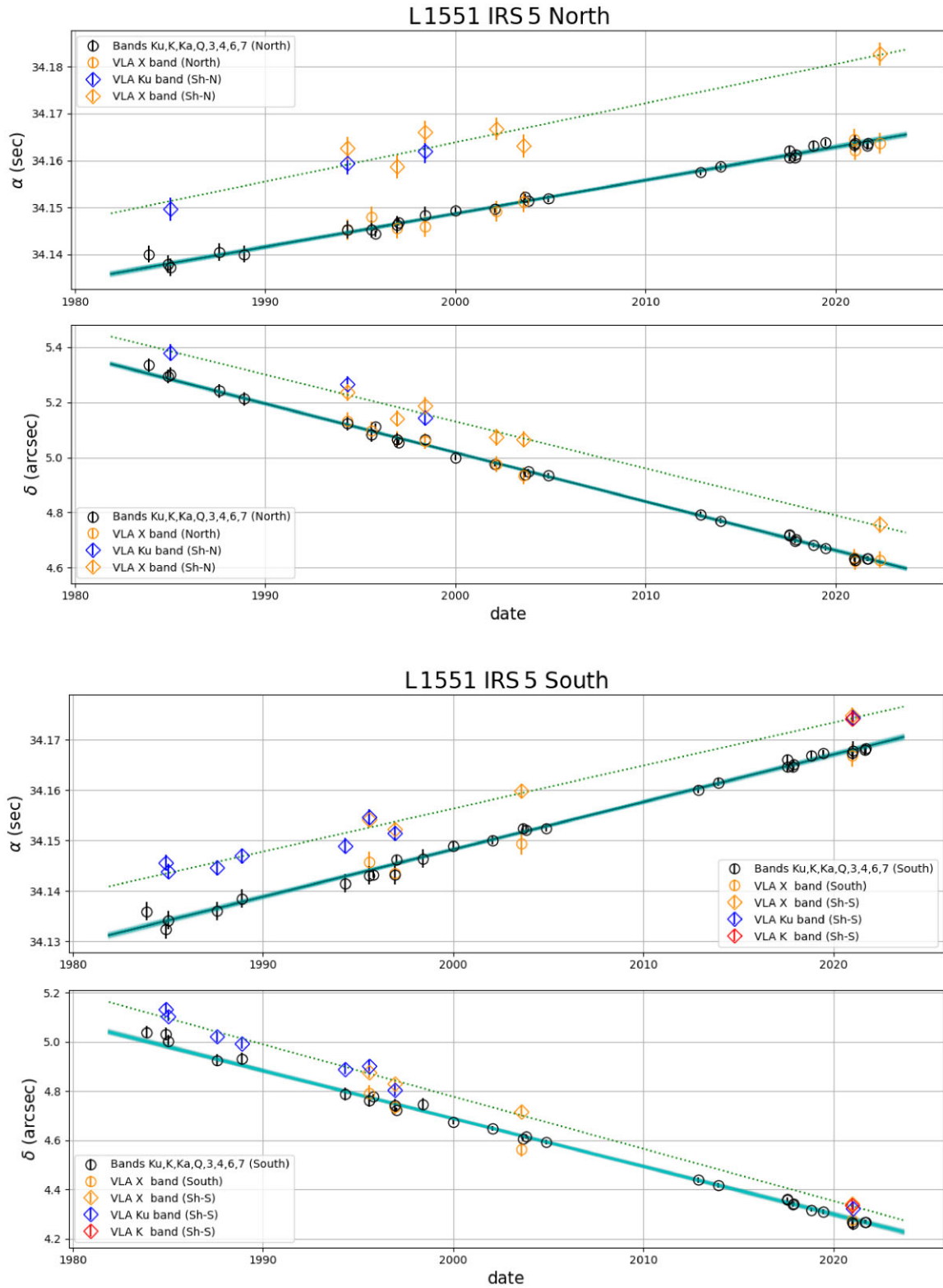


Figure 2. Position as a function of time of L 1551 IRS 5 N (top) and L 1551 IRS 5 S (bottom) after applying all astrometric corrections (gain calibrator positions and trigonometric parallax) for all observations considered in this paper. Black symbols indicate the positions considered in Fig. 1, while the other colours and symbols are defined in the legends. The display schemes for the fits to L 1551 IRS 5 N and S are the same as in Fig. 1. The dotted line shows the fit to the positions of Sh-N and Sh-S.

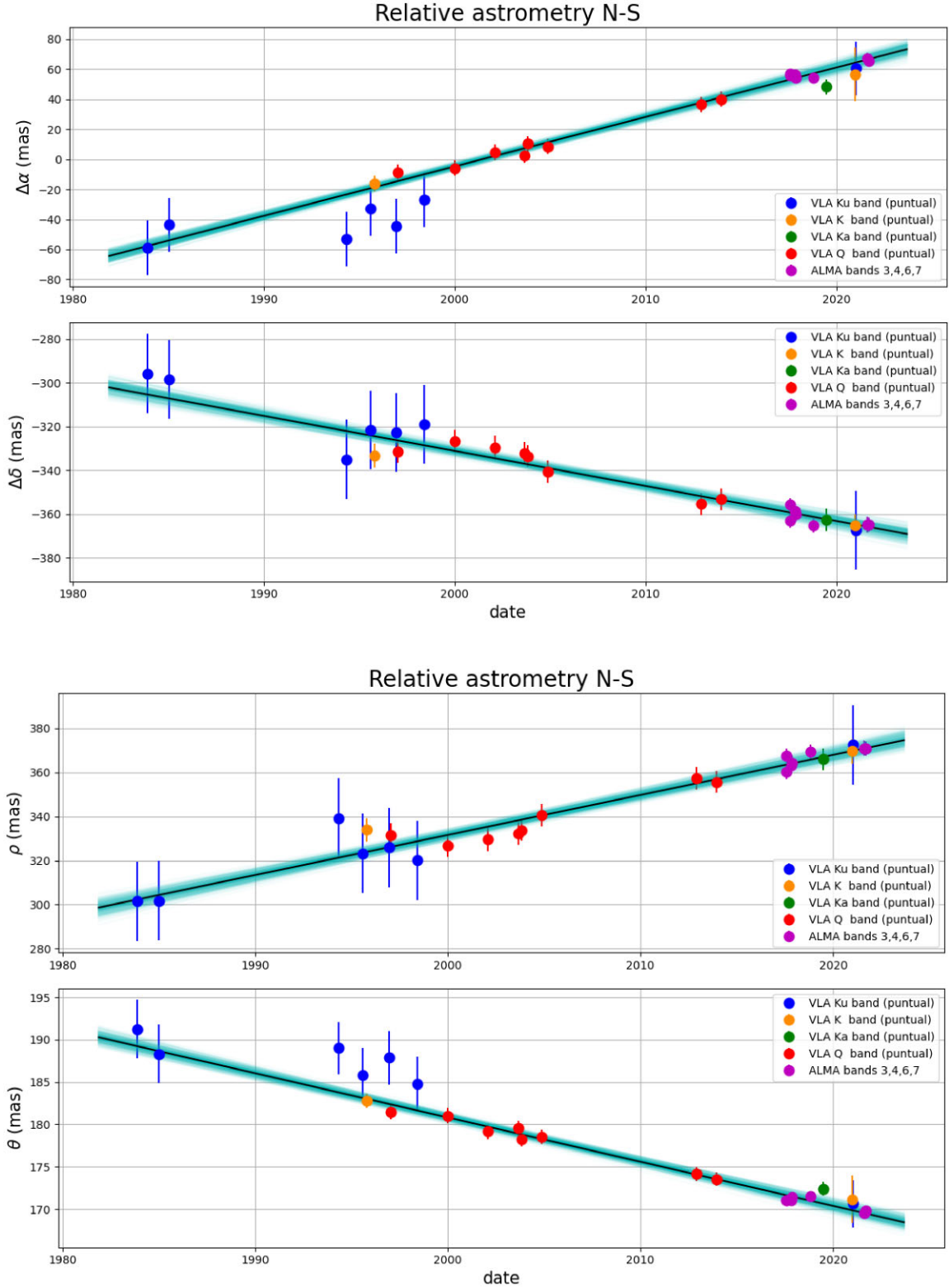


Figure 3. Relative positions between L 1551 IRS 5 N and S as a function of time. The first two panels show the relative right ascension and declination between the sources, while the following two show their separation and position angle. The best fits are shown following the same strategy as in Figs 1 and 2.

useful to point out that the relative proper motions ($2\text{--}3 \text{ mas yr}^{-1}$) are almost one order of magnitude smaller than the absolute proper motions ($10\text{--}20 \text{ mas yr}^{-1}$). Thus, the error bars in Fig. 3, although intrinsically smaller than those in Figs 1 and 2, represent a larger

percentage of the underlying proper motion. The values obtained here for the relative proper motions between L 1551 IRS 5 N and S are consistent with those reported by Rodríguez et al. (2003a) and Villa et al. (2017) but they are five to six times more accurate. Finally,

we note that, given the distance to the system (146.4 ± 0.5 pc; Galli et al. 2018), the relative proper motion between L 1551 IRS 5 N and S corresponds to the relative transverse velocity of about 2.5 km s^{-1} . This is comparable to the difference in radial velocity known to exist between the two sources ($\approx 3 \text{ km s}^{-1}$; Bianchi et al. 2020).

4 DISCUSSION

4.1 Interpretation of the absolute proper motions

We can obtain a good estimate of the absolute proper motion of the binary system L 1551 IRS 5 by taking the (simple) average of the absolute proper motions of L 1551 IRS 5 N and S. Since accelerations are not significant, here we use the results of the fits with linear and uniform proper motions reported in Table 4. We obtain:

$$\mu_{\alpha} \cos \delta = +11.75 \pm 0.20 \text{ mas yr}^{-1} \quad (23)$$

$$\mu_{\delta} = -18.60 \pm 0.21 \text{ mas yr}^{-1}. \quad (24)$$

This corresponds to a total proper motion $\mu_{\text{tot}} = 22.00 \pm 0.20 \text{ mas yr}^{-1}$ and, considering the distance to the system of 146.4 ± 0.5 pc (Galli et al. 2018), to a velocity on the plane of the sky of $15.27 \pm 0.15 \text{ km s}^{-1}$. The proper motions measured by the VLA and ALMA are registered relative to the barycenter of the solar system, so the velocity quoted above is, almost exactly, measured in the heliocentric system. The systemic radial velocity of L 1551 IRS 5, estimated from molecular lines, is $v_{\text{lsr}} = 6.0 \pm 0.1 \text{ km s}^{-1}$ (Bianchi et al. 2020); in the heliocentric system, this corresponds to $v_{\text{hel}} = 16.6 \pm 0.1 \text{ km s}^{-1}$.

One can estimate which fraction of the proper motion and radial velocity is due to the peculiar motion of the Sun (i.e. to the motion of the Sun relative to its LSR) and which fraction is caused by the peculiar motion of L 1551 IRS 5 itself. For this, we calculate the projections of the solar motion on the right ascension and declination axes and along the line of sight towards L 1551 IRS 5; we adopt the values of the solar motion measured by Schönrich, Binney & Dehnen (2010): ($U_{\odot} = 11.1$, $V_{\odot} = 12.24$, $W_{\odot} = 7.25$) km s^{-1} . We obtain that, if L 1551 IRS 5 were at rest relative to its LSR, its proper motions would be $\mu_{\alpha} \cos \delta = +6.2 \text{ mas yr}^{-1}$ and $\mu_{\delta} = -17.0 \text{ mas yr}^{-1}$, while its heliocentric radial velocity would be 12.7 km s^{-1} . Thus, the peculiar proper motion of L 1551 IRS 5 is only $\mu_{\alpha, \text{pec}} \cos(\delta) = +5.5 \text{ mas yr}^{-1}$ and $\mu_{\delta, \text{pec}} = -1.6 \text{ mas yr}^{-1}$, while the peculiar radial velocity is 3.9 km s^{-1} . This corresponds to a peculiar velocity on the plane of the sky of 4.0 km s^{-1} and a total peculiar velocity (including the radial component) of 5.6 km s^{-1} .

The previous calculation indicates that the peculiar velocity components of L 1551 IRS 5 in the plane of the sky (4.0 km s^{-1}) and along the line of sight (3.9 km s^{-1}) are much smaller than the corresponding values for the total heliocentric motion (15.27 and 16.6 km s^{-1} , respectively): the peculiar motion of the Sun dominates the heliocentric motion of L 1551 IRS 5. This behaviour is typical of Taurus and other star-forming regions (e.g. Reid et al. 2009, 2014; Rivera et al. 2015) and is dynamically expected. Young stars form out of interstellar gas which, because of its internal viscosity, tends to move along circular orbits about the Galactic centre (Binney & Merrifield 1998). As a result, young stars just after their formation are expected to have small peculiar velocities. In the case of the Taurus complex, where L 1551 IRS 5 resides, a large scale rotation contributes to the net peculiar velocity (Rivera et al. 2015).

4.2 The possible nature of Sh-N and Sh-S

As we have already mentioned and can be seen in the images of Appendix A, Sh-N and Sh-S are increasingly prominent at lower frequencies, so they are most likely produced by free-free emission. Sh-N is located at a position angle relative to L 1551 IRS 5 N of $64.16 \pm 5.70^{\circ}$, consistent with the direction of the jet driven by that protostar as reported by Rodríguez et al. (2003b). Similarly, Sh-S is located at a position angle relative to L 1551 IRS 5 S of $53.60 \pm 5.40^{\circ}$, consistent with the direction of the jet driven by that protostar as also reported by Rodríguez et al. (2003b). We conclude that Sh-N and Sh-S are most likely shock features along the jets driven by L 1551 IRS 5 N and S, respectively. Interestingly, however, their proper motions are very similar to those of L 1551 IRS 5 N and S. From the absolute proper motions determined in Section 3.1, we obtain the following relative proper motions between Sh-N and N, and between Sh-S and S, respectively:

$$\Delta(\mu_{\alpha} \cos \delta) = +1.93 \pm 1.41 \text{ mas yr}^{-1} \quad (\text{Sh} - \text{N}) \quad (25)$$

$$\Delta(\mu_{\delta}) = +0.68 \pm 1.11 \text{ mas yr}^{-1} \quad (\text{Sh} - \text{N}), \quad (26)$$

and

$$\Delta(\mu_{\alpha} \cos \delta) = -1.26 \pm 0.41 \text{ mas yr}^{-1} \quad (\text{Sh} - \text{S}) \quad (27)$$

$$\Delta(\mu_{\delta}) = -1.70 \pm 0.41 \text{ mas yr}^{-1} \quad (\text{Sh} - \text{S}). \quad (28)$$

This implies that Sh-N is moving away from L 1551 IRS 5 N at $2.05 \pm 1.38 \text{ mas yr}^{-1}$ ($1.43 \pm 0.96 \text{ km s}^{-1}$, given the distance to the system), whereas Sh-S is moving toward L 1551 IRS 5 S at $2.12 \pm 0.41 \text{ mas yr}^{-1}$ ($1.48 \pm 0.26 \text{ km s}^{-1}$). These values are much smaller than the speed of jets driven by low-mass stars (tens to hundreds of km s^{-1}) and indicate that Sh-N and Sh-S are nearly stationary relative to their respective driving sources. The conclusion that Sh-S appears may be approaching L 1551 IRS 5 S is surprising but should also be considered cautiously. First, the approaching motion is only detected at the 5σ level; secondly, Sh-S is an extended and variable feature so its astrometry is less reliable than that of compact sources.

It is interesting to discuss the nature of Sh-N and Sh-S in light of their characteristics determined here. Shocks are, of course, often present around low-mass young stellar objects, particularly along their jets, but they tend to move away from the driving central protostars with velocities of tens or hundreds of km s^{-1} , comparable with that of the jets themselves (e.g. Curiel et al. 2006). Stationary features such as those documented here are unusual, although not unheard of – Carrasco-González et al. (2021) reported on such features in the higher mass protostellar system Cep A HW2. Additional work, both observational and theoretical, will be needed to ascertain the nature of Sh-N and Sh-S, but the possibility of a collimation or re-collimation (or re-confinement) feature is perhaps worth mentioning here. These features occur when outflowing material originally moving roughly radially away from the central protostar is (re-)confined due to external pressure (either from ambient material or from a more massive but slower wind) or an external magnetic field. They have been well-documented in extragalactic jets (e.g. Sanders 1983; Gourgouliatos & Komissarov 2018) where they typically form along the jet axis. Their potential existence in young stellar systems has been considered by Günther, Li & Schneider (2014), who argued that they could help explain a peculiar X-ray feature in DG Tau. Carrasco-González et al. (2021) also invoked such a mechanism to explain stationary shock features in Cep A HW2.

4.3 L 1551 IRS 5 mass estimates

As mentioned in Section 1, Rodríguez et al. (2003a) and, more recently, Villa et al. (2017) estimated the mass of L 1551 IRS 5 using the following strategy. They assumed a circular orbit with the same inclination relative to the plane of the sky, $i = 60^\circ$, as the circumstellar discs surrounding the individual protostars (Rodríguez et al. 1998; Chou et al. 2014). They further assumed that the orbit was oriented exactly in the N–S direction as suggested by early observations of the circumstellar discs (Rodríguez et al. 1998). Under these assumptions, the orbit projected on the plane of the sky has an axis ratio of 2 ($\cos 60^\circ = 0.5$) and a position angle of 180° . Given that the position angle between L 1551 IRS 5 N and S was of the order of 180° during their observations, Rodríguez et al. (2003a) and Villa et al. (2017) concluded that their data traced the system during its maximum elongation on the plane of the sky. In this situation and given the assumption of the model, the current projected separation corresponds to the true radius of the orbit, while the relative velocity measured on the plane of the sky, V_m , corresponds to the true circular velocity, V_c , corrected for the inclination: $V_m = V_c \cos i$. They used the average separation between the sources during their observations as the radius of the orbit, and the relative proper motions to deduce the relative velocity. Rodríguez et al. (2003a) obtained a mass of $1.3 M_\odot$, while Villa et al. (2017) obtained $1.9 M_\odot$.¹ As they noticed, these values are comparable to the typical masses of more evolved T Tauri binary systems (Ghez et al. 1995; Woitas, Leinert & Köhler 2001).

As a first step, and to check for consistency, we can repeat the treatment of Rodríguez et al. (2003a) and Villa et al. (2017) using our more extensive data set. We will also use the most recent distance determination to L 1551 IRS 5: 146.4 ± 0.5 pc (Galli et al. 2018). From the measured relative proper motions (Section 3.2), we can infer the relative projected velocity between the sources to be 2.54 ± 0.07 km s⁻¹. Under our assumptions, this leads to a deprojected relative velocity of 5.08 ± 0.14 km s⁻¹. The mean separation between the sources in our observations, which we take as the true radius of the circular orbit, is 345 ± 22 mas, or 50.5 ± 3.2 au. Combining the deprojected velocity and true radius of the orbit, we arrive at an orbital period of 296 ± 20 yr. Finally, Kepler’s law yields a mass of $1.5 \pm 0.2 M_\odot$ for the L 1551 IRS 5 system. This value is intermediate between the figures reported by Rodríguez et al. (2003a) and Villa et al. (2017). It is important to caution about the relevance of the uncertainties reported in the previous calculation: it results from propagating the errors on the separation, proper motions, and distance, but does not include any contribution accounting for our somewhat arbitrary choice of model: a circular orbit with an inclination of 60° at a position angle of 180° .

Fig. 3 shows that the separation between the two sources in L 1551 IRS 5 keeps increasing even after their relative position angle becomes larger than 180° . This clearly indicates that the description model used in the previous paragraph is not entirely adequate. Following Lim & Takakuwa (2006), we now consider the next simplest model: a circular orbit with the same inclination ($i = 60.5^\circ$) and position angle (P.A. = 161.5°) as the circumbinary disc around L 1551 IRS 5 (Cruz-Sáenz de Miera et al. 2019; Takakuwa et al. 2020). We use the parameters of the circumbinary disc, rather than the circumstellar discs, because it is very well resolved in ALMA observations, so the parameters are well constrained. As in the previous case, with this choice of description model, the only free parameters are the radius and period of the orbit. To obtain them, we deprojected the observed positions to obtain their (x, y) coordinates

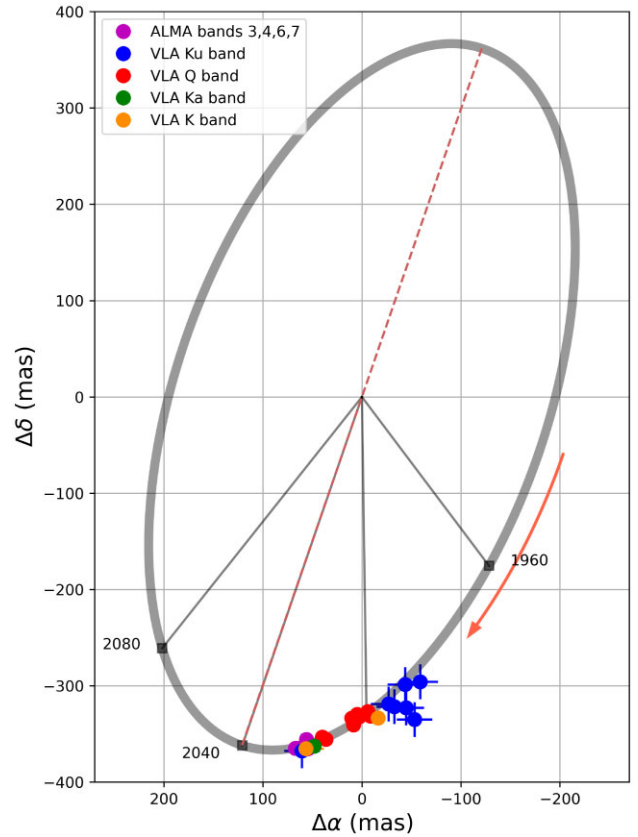


Figure 4. Orbit fitting the measured relative positions, assuming the same orientation and position angle as the circumbinary disc. The dashed line shows the major axis, and the direction of rotation is indicated by the arrow. Predicted relative positions for years 1960, 2040, and 2080, according to this model, are also indicated.

in the plane of the orbit. The radius of the orbit is then simply the mean separation between the two stars in that (x, y) coordinate system – we obtain $R = 381.6 \pm 13.6$ mas, or 55.9 ± 2.0 au. To obtain the orbital period, we fitted the position angle between the two sources in the (x, y) plane, ϕ , as a function of time to constrain the rate of change of that position angle. We obtain $|\dot{\phi}| = 0.88 \pm 0.03^\circ$ yr⁻¹. We emphasize that ϕ is measured in the plane of the orbit, while θ is in the plane of the sky; this explains why the value of $|\dot{\phi}|$ reported here is different from the value of $|\dot{\theta}|$ quoted earlier. The value of $|\dot{\phi}|$ implies an orbital period of 407 ± 13 yr. The corresponding orbit is shown as a grey ellipse in Fig. 4. From Kepler’s law, we finally obtain, for this description model of the orbit, a mass of $1.0 \pm 0.1 M_\odot$. Once again, the error quoted here only accounts for the observational uncertainties, not for the errors associated with our particular choice of orbit. We note that a value of $1.0 M_\odot$ is consistent with the C¹⁸O position–velocity diagram tracing the kinematics of the circumbinary disc (A. Duran et al., in preparation).

Finally, we have used a more rigorous approach, modelling the relative motion between L 1551 IRS 5 N and S using an MCMC orbit-fitting algorithm as implemented in the ORBITIZE! package (Blunt et al. 2017, 2020). The left panel of Fig. 5 shows a set of 2000 orbits drawn from the posteriors, while the right panel shows two graphs corresponding to the separation angle and position angle with respect to time. The orbital parameters calculated by this method were the semimajor axis (a), the eccentricity (e), the inclination (i),

Table 5. Results obtained from ORBITIZE!.

Parameter	Value	Units
a	44.0 ± 3.2	AU
e	0.27 ± 0.09	
Ω	161.3 ± 4.1	degrees
i	126.3 ± 5.0	degrees
ω	175.9 ± 15.1	degrees
T_0	2457329 ± 28	
P	300 ± 38	years
Total mass	0.96 ± 0.17	M_{\odot}

the argument of periastron (ω), the position angle of nodes (Ω), and the epoch of periastron passage (T_0) which are shown in Table 5 and Fig. 6. We used a total of 10 000 walkers and 500 burning steps. The fits behave as expected: the orbit is reasonably well constrained near the observed position but diverge quickly far from our observations. This same effect is even visible within our observing span. The right panel of Fig. 5 clearly shows that the fits are better constrained near the most recent observations, while there is more dispersion at the earlier observed epochs. This is because the most recent observations have higher astrometric accuracy, and there is also a greater number of observations made at 7 mm from the VLA, in addition to the ALMA observations.

The mass obtained from ORBITIZE! ($0.96 \pm 0.17 M_{\odot}$) is in good agreement with those measured above assuming circular orbits. We argue, however, that the errors reported in this case are more realistic as they account for uncertainties on all orbital parameters. We note also that the eccentricity (0.27 ± 0.09) is modest as expected from dynamical constraints (Pichardo et al. 2005). Lim et al. (2016) arrived at a similar conclusion by imposing constraints from tidal truncation. The mass determined in this work is more accurate than those previously published because it is based on a significantly larger data set and uses an accurate distance to the target.

4.4 Comments on combining heterogeneous interferometric data and future measurements

Radio-interferometers can provide accurate astrometry (Reid & Honma 2014) but, as mentioned in Section 1, combining heterogeneous interferometric data requires care. If multiple gain calibrators (possibly with changing or erroneous catalogued positions) and multiple instruments are used, steps must be taken to ensure that all positions are consistently registered on a common astrometric reference frame. In addition, multiple frequencies can trace different physical components in a system, so the positions should not be blindly combined. In this paper, we showed that, if proper measures are taken to enforce the homogeneity of the astrometry, one can combine data collected over several decades with different instruments and multiple gain calibrators to obtain high accuracy absolute astrometry (Fig. 1). This is, in large part, the consequence of decade-long efforts to refine the positions of hundreds of gain calibrators (Johnston et al. 1995; Beasley et al. 2002). In turn, accurate astrometry can enable a direct identification of the various sources in a given system (Fig. 2), contributing to the possibility of combining more data in a meaningful manner.

The possibility of combining heterogeneous interferometric data for astrometric purposes opens interesting possibilities. The VLA already includes more than four decades of usable data, while ALMA is reaching its first complete decade of regular observing and is anticipated to keep operating for at least two more decades. The Square Kilometer Array (SKA; Dewdney et al. 2009) and the next-generation VLA (ngVLA; Murphy et al. 2018) are also now on the horizon and should be operating until well into the second half of the 21st century. Combining data from these instruments ought to eventually enable the astrometric monitoring of interesting targets for a full century. In the specific case of L 1551 IRS 5, given the orbital period of ~ 300 yr (Section 4.3), it will become possible to constrain the mass quite accurately, as we will show in the next paragraph. For reference, we indicate the expected relative positions of the two protostars in the system in 2040 and 2080 in Fig. 4.

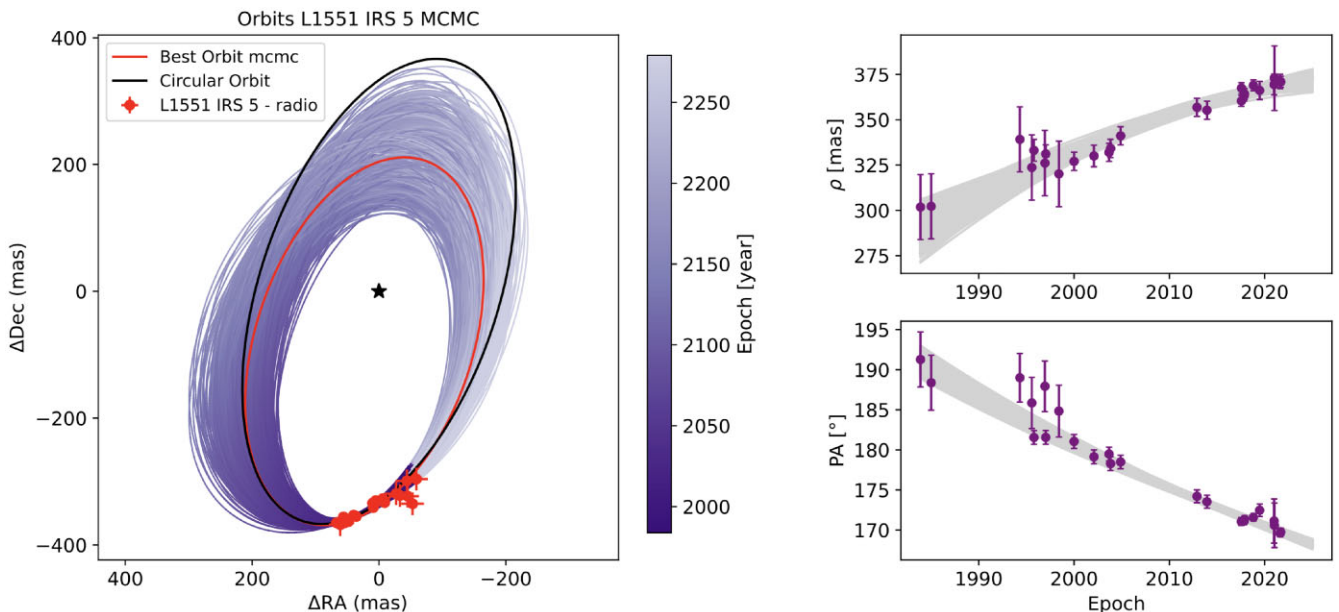


Figure 5. Best MCMC fits to the relative positions obtained from the ORBITIZE! package. The left panel shows the orbits on the plane of the sky, while the right panels show the separation and angular position as a function of time. Two thousand possible orbits drawn from the MCMC posteriors are shown as semitransparent violet lines. The orbit corresponding to the parameters listed in Table 5 is shown in red, while the best circular orbit discussed in Section 4.3 is shown in black.

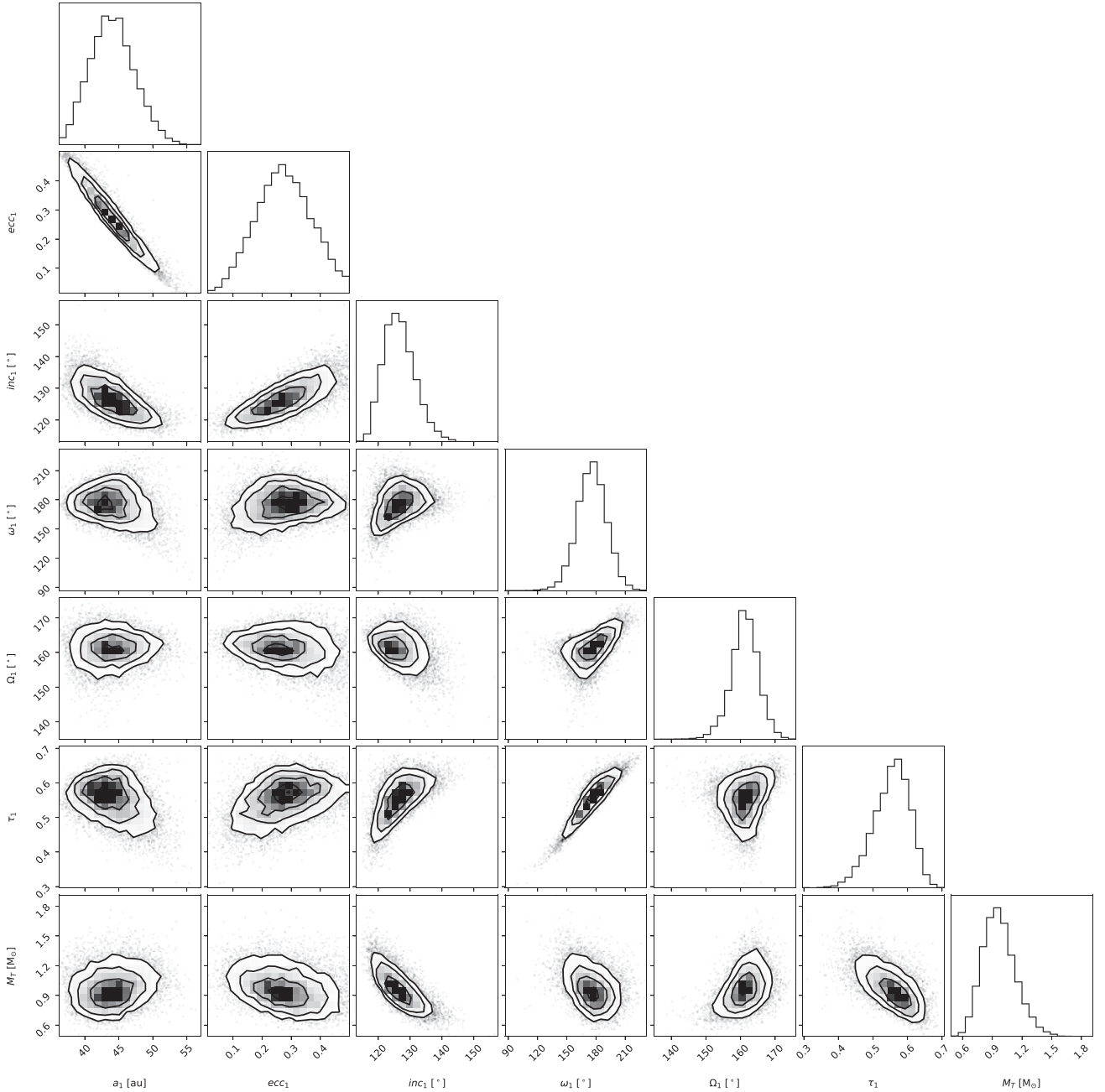


Figure 6. Corner plots indicating the posterior distributions on each of the parameters fitted by the MCMC package ORBITIZE!.

To assess quantitatively the impact of future observations, we ran the following simulation. We assumed L 1551 IRS 5 would be observed roughly every two years from 2024 until 2080 (we included a random component in the scheduling to mimic realistic observations). Adopting the best orbit obtained by ORBITIZE! (Section 4.3), we calculated the expected relative position of the two protostars in L 1551 IRS 5 at these epochs and generated synthetic observations by adding a noise term with a dispersion of 5 mas in each direction (RA and Dec). We then used ORBITIZE! again to fit an orbit to the actual VLA/ALMA measurements reported here supplemented by these 56 yr of simulated additional observations. The mass determined in this way has an error of $0.04 M_{\odot}$, or 4 per cent, compared with

the uncertainty of 18 per cent ($0.17 M_{\odot}/0.96 M_{\odot}$) currently. We note, however, that the determination of the eccentricity is only marginally improved by the inclusion of additional data. From the same model, we also generated simulated absolute positions, assuming the proper motions determined in Section 3.1 for L 1551 IRS 5 N and S, and a mass ratio of 3 between the two stars. We then fitted these positions with an accelerated proper motion model. The addition of simulated data extending to 2080 makes it possible to detect the acceleration terms at the 3–5 sigma levels in right ascension and 7–12 sigma levels in declination (for that specific portion of the L 1551 IRS 5 orbit, the acceleration signal is higher in declination than right ascension). The ratio between the accelerations of L 1551 IRS 5 N and S enables the

recovery of the mass ratio at a high level of significance: from the simulation, we obtain a mass ratio of 2.9 ± 0.5 , compared with the input simulation value of 3.

In summary, our simulations demonstrate that adding several decades of high quality observations of L 1551 IRS 5 with ALMA, the ngVLA or the SKA would improve very significantly the accuracy of the system mass measurement (by a factor of several) and would enable, for the first time, a reliable estimate of the mass ratio. Of course, the same would be true for other protostellar systems (e.g. L 1551 NE or VLA 1623) for which archival VLA and ALMA data going back several decades already exist. For similar systems which have not been regularly observed with the VLA in the last decades, new observations with existing and planned interferometers would provide total mass measurements in a few decades, by mass ratio estimates will require more patience.

4.5 General implications for protostellar systems

The formation of binary stellar systems can occur through two main (and not mutually exclusive) modes: turbulent fragmentation of the parental core (e.g. Padoan et al. 2007) and gravitational disc fragmentation (Adams, Ruden & Shu 1989). These two scenarios make clearly distinct predictions on the architectures of the resulting systems. As discussed in details by Lim & Takakuwa (2006) and Lim et al. (2016), the properties of L 1551 IRS 5 are fully consistent with a disc fragmentation origin. The relevant architectural properties include the near alignment between the circumstellar and circumbinary discs and the binary orbital plane, confirmed here by the ORBITIZE! results which indicate an inclination of the orbital plane of $126.3 \pm 5.7^\circ$ ($= -53.7 \pm 5.7^\circ$), consistent within one sigma with the 60.5° inclination of the circumbinary disc. The situation in other systems, however, is often less clear. To mention but one example, the circumstellar discs in the VLA 1623 compact quadruple system in Ophiuchus are clearly not aligned with one another (Mercimek et al. 2023, and references therein). Constraining the orbital architecture of binary and multiple systems using long-scale astrometric monitoring studies similar to that presented here for L 1551 IRS 5 is critical to better understanding their formation mechanisms.

A related issue concerns the impact of binarity on the discs and jets in protostellar systems (Reipurth et al. 2014; Sheikhezami & Sepahvand 2024; and references therein). A well-known effect is tidal disc truncation (Artymowicz & Lubow 1994), but subtler consequences, such as the creation of spiral patterns can also occur. The non-axisymmetry of the circumstellar disc in L 1551 IRS 5 has recently been interpreted as a result of the binarity of the central source by N. Cuello et al. (in preparation). For the modelling of these effects, the mass of the system and the size of the orbit are important, but the mass ratio and the eccentricity are also crucial. As we have shown here, current and future astrometric monitoring studies can provide these parameters with good accuracy; they can therefore contribute uniquely to studies of the impact of binarity on early stellar evolution.

5 CONCLUSIONS AND PERSPECTIVES

We have presented a detailed study of the astrometry of the Class I protostellar system L 1551 IRS 5 based on nearly forty years of VLA and ALMA observations. The absolute proper motions of the protostars in the system were determined with an accuracy of the order of 0.2 mas yr^{-1} – a one order of magnitude improvement over previous determinations (Section 3.1). These absolute proper motions show that, while the emission at frequencies higher than

about 20 GHz directly trace the protostars or their immediate environments, the emission at frequencies below about 15 GHz includes a significant contribution from the larger scale jets. In particular, we identify compact emission sources located about 0.1 arcsec to the north-east of L 1551 IRS 5 N and S, associated with what appear to be nearly stationary shock features. Our data also enabled us to track the relative proper motions between the two protostars in the system with an accuracy three to five times better than previous studies (Section 3.2). In turn, this allowed us to monitor the orbital motion in the system and constrain its mass ($0.96 \pm 0.17 M_\odot$) and the eccentricity of the orbit (0.27 ± 0.09). Continued observations in the coming decades ought to progressively improve the mass determination of L 1551 IRS 5, and will eventually enable a measurement of the mass ratio. Other similar systems nearby binary and multiple protostellar systems (such as L 1551 NE or VLA 1623) can be monitored similarly and this would have important implications on studies of the impact of binarity on early stellar evolution.

ACKNOWLEDGEMENTS

We would like to thank the referee for comments and suggestions for this work. RHG thanks to ‘Consejo Nacional de Ciencia y Tecnología’ (CONACYT) for grant 756285. LL acknowledges the support of ‘Dirección General de Asuntos del Personal Académico de la Universidad Nacional Autónoma de México, Programa de Apoyo a Proyectos de Investigación e Innovación Tecnológica’ (UNAM-DGAPA, PAPIIT) grants IN112820 and IN108324, and ‘Consejo Nacional de Humanidades, Ciencias y Tecnologías’ CONACYT-CF grant 263356. CC-G acknowledges support from UNAM DGAPA-PAPIIT grant IG101224 and from CONAHCyT Ciencia de Frontera project ID 86372. LFR acknowledges the financial support of UNAM-DGAPA PAPIIT grant IN108920. AR acknowledges support from the UNAM-DGAPA PAPIIT grant IG100422. SAD acknowledges the M2FINDERS project from the European Research Council (ERC) under the European Union’s Horizon 2020 research and innovation programme (grant no. 101018682). EB acknowledges the Deutsche Forschungsgemeinschaft (DFG, German Research Foundation) under Germany’s Excellence Strategy – EXC 2094–390783311. AFJ acknowledges support from National Astronomical Observatory of Japan (NAOJ) ALMA Scientific Research Grant code 2019-13B. This project has received funding from the European Research Council (ERC) under the European Union Horizon Europe programme (grant agreement No. 101042275, project StellarMADE).

DATA AVAILABILITY

All position tables are available in machine-readable format.

REFERENCES

- Adams F. C., Lada C. J., Shu F. H., 1987, *ApJ*, 312, 788
- Adams F. C., Ruden S. P., Shu F. H., 1989, *ApJ*, 347, 959
- Anglada G., Rodríguez L. F., Carrasco-González C., 2018, *A&AR*, 26, 3
- Artymowicz P., Lubow S. H., 1994, *ApJ*, 421, 651
- Barron E., Kaplan G., Bangert J., Bartlett J., Puatua W., Harris W., Barrett P., 2011, in American Astronomical Society Meeting Abstracts #217, 344.14
- Beasley A. J., Gordon D., Peck A. B., Petrov L., MacMillan D. S., Fomalont E. B., Ma C., 2002, *ApJS*, 141, 13
- Bianchi E. et al., 2020, *MNRAS*, 498, L87

- Bieging J., Cohen M., 1985, in Verschuur G. L., Kellermann K. I., eds, *Galactic and Extragalactic Radio Astronomy: Radio Stars*. Springer, New York, p. 101
- Binney J., Merrifield M., 1998, *Galactic Astronomy*. Princeton Univ. Press, Princeton
- Blunt S. et al., 2017, *AJ*, 153, 229
- Blunt S. et al., 2020, *AJ*, 159, 89
- Carrasco-González C., Sanna A., Rodríguez-Kamenetzky A., Moscadelli L., Hoare M., Torrelles J. M., Galván-Madrid R., Izquierdo A. F., 2021, *ApJ*, 914, L1
- Chandler C. J., Brogan C. L., Shirley Y. L., Loinard L., 2005, *ApJ*, 632, 371
- Chou T.-L., Takakuwa S., Yen H.-W., Ohashi N., Ho P. T., 2014, *ApJ*, 796, 70
- Codella C., Ceccarelli C., Chandler C., Sakai N., Yamamoto S., FAUST Team, 2021, *Front. Astron. Space Sci.*, 8, 227
- Condon J. J., 1997, *PASP*, 109, 166
- Cruz-Sáenz de Miera F., Kóspál Á., Abraham P., Liu H. B., Takami M., 2019, *ApJ*, 882, L4
- Curiel S. et al., 2006, *ApJ*, 638, 878
- Dewdney P. E., Hall P. J., Schilizzi R. T., Lazio T. J. L. W., 2009, *IEEE Proc.*, 97, 1482
- Dzib S. A. et al., 2017, *ApJ*, 834, 139
- Feeney-Johansson A. et al., 2023, *A&A*, 677, A97
- Fridlund C. V. M., Liseau R., 1998, *ApJ*, 499, L75
- Galli P. A. B. et al., 2018, *ApJ*, 859, 33
- Galli P. et al., 2019, *A&A*, 630, A137
- Ghez A. M., Weinberger A. J., Neugebauer G., Matthews K., McCarthy D. W. J., 1995, *AJ*, 110, 753
- Gourgouliatos K. N., Komissarov S. S., 2018, *Nat. Astron.*, 2, 167
- Günther H. M., Li Z.-Y., Schneider P. C., 2014, *ApJ*, 795, 51
- Hayashi M., Pyo T.-S., 2009, *ApJ*, 694, 582
- Hernández-Gómez A. et al., 2019, *ApJ*, 875, 94
- Itoh Y. et al., 2000, *PASJ*, 52, 81
- Johnston K. J. et al., 1995, *AJ*, 110, 880
- Lim J., Takakuwa S., 2006, *ApJ*, 653, 425
- Lim J., Yeung P. K. H., Hanawa T., Takakuwa S., Matsumoto T., Saigo K., 2016, *ApJ*, 826, 153
- Loinard L., 2002, *Rev. Mex. Astron. Astrofis.*, 38, 61
- Loinard L., Chandler C. J., Rodríguez L. F., D'Alessio P., Brogan C. L., Wilner D. J., Ho P. T. P., 2007, *ApJ*, 670, 1353
- Looney L. W., Mundy L. G., Welch W., 1997, *ApJ*, 484, L157
- Looney L. W., Mundy L. G., Welch W. J., 2000, *ApJ*, 529, 477
- Lynds B. T., 1962, *ApJS*, 7, 1
- Maureira M. J., Pineda J. E., Segura-Cox D. M., Caselli P., Testi L., Lodato G., Loinard L., Hernández-Gómez A., 2020, *ApJ*, 897, 59
- McMullin J., Waters B., Schiebel D., Young W., Golap K., Shaw R., Hill F., Bell D., 2007, in Shaw R. A., Hill F., Bell D. J., eds, *ASP Conf. Ser. Vol. 376, Astronomical Data Analysis Software and Systems XVI*. Astron. Soc. Pac., San Francisco, p. 127
- Mercimek S. et al., 2023, *MNRAS*, 522, 2384
- Murphy E. J. et al., 2018, in Murphy E., ed., *ASP Conf. Ser. Vol. 517, Science with a Next Generation Very Large Array*. Astron. Soc. Pac., San Francisco, p. 3
- Napier P. J., Bagri D. S., Clark B. G., Rogers A. E. E., Romney J. D., Thompson A. R., Walker R. C., 1994, *IEEE Proc.*, 82, 658
- Padoan P., Nordlund Å., Kritsuk A. G., Norman M. L., Li P. S., 2007, *ApJ*, 661, 972
- Perley R. A., Chandler C. J., Butler B. J., Wrobel J. M., 2011, *ApJ*, 739, L1
- Pichardo B., Sparke L. S., Aguilar L. A., 2005, *MNRAS*, 359, 521
- Reid M. J., Honma M., 2014, *ARA&A*, 52, 339
- Reid M. J. et al., 2009, *ApJ*, 700, 137
- Reid M. J. et al., 2014, *ApJ*, 783, 130
- Reipurth B., Clarke C. J., Boss A. P., Goodwin S. P., Rodríguez L. F., Stassun K. G., Tokovinin A., Zinnecker H., 2014, in Beuther H., Klessen R. S., Dullemond C. P., Henning T., eds, *Protostars and Planets VI*. Univ. Arizona Press, Tucson, p. 267
- Rivera J. L., Loinard L., Dzib S. A., Ortiz-León G. N., Rodríguez L. F., Torres R. M., 2015, *ApJ*, 807, 119
- Rodríguez L. et al., 1998, *Nature*, 395, 355
- Rodríguez L. F., Curiel S., Cantó J., Loinard L., Raga A. C., Torrelles J. M., 2003a, *ApJ*, 583, 330
- Rodríguez L. F., Porras A., Claussen M. J., Curiel S., Wilner D. J., Ho P. T. P., 2003b, *ApJ*, 586, L137
- Sanders R. H., 1983, *ApJ*, 266, 73
- Schönrich R., Binney J., Dehnen W., 2010, *MNRAS*, 403, 1829
- Seidelmann P. K., 1992, in *Explanatory Supplement to the Astronomical Almanac. A revision to the Explanatory Supplement to the Astronomical Ephemeris and the American Ephemeris and Nautical Almanac*. University Science Books, New York
- Sheikhnezami S., Sepahvand M., 2024, *ApJ*, 966, 82
- Strom K. M., Strom S. E., Vrba F. J., 1976, *AJ*, 81, 320
- Takakuwa S. et al., 2020, *ApJ*, 898, 10
- The CASA Team, 2022, *PASP*, 134, 114501
- Villa A. M., Trinidad M. A., de la Fuente E., Rodríguez-Esnard T., 2017, *Rev. Mex. Astron. Astrofis.*, 53, 525
- Woitas J., Leinert C., Köhler R., 2001, *A&A*, 376, 982

APPENDIX A: VLA IMAGES OF L 1551 IRS 5

Figure A1 shows the resulting images of L1551 IRS 5 from the VLA observations that were used for this work. Each image was shifted according to the corrections applied to the positions mentioned in Section 2.2, and are shown in the chronological order of observation, to appreciate the projected motion of L1551 IRS 5 that goes in the North-South and West-East directions.

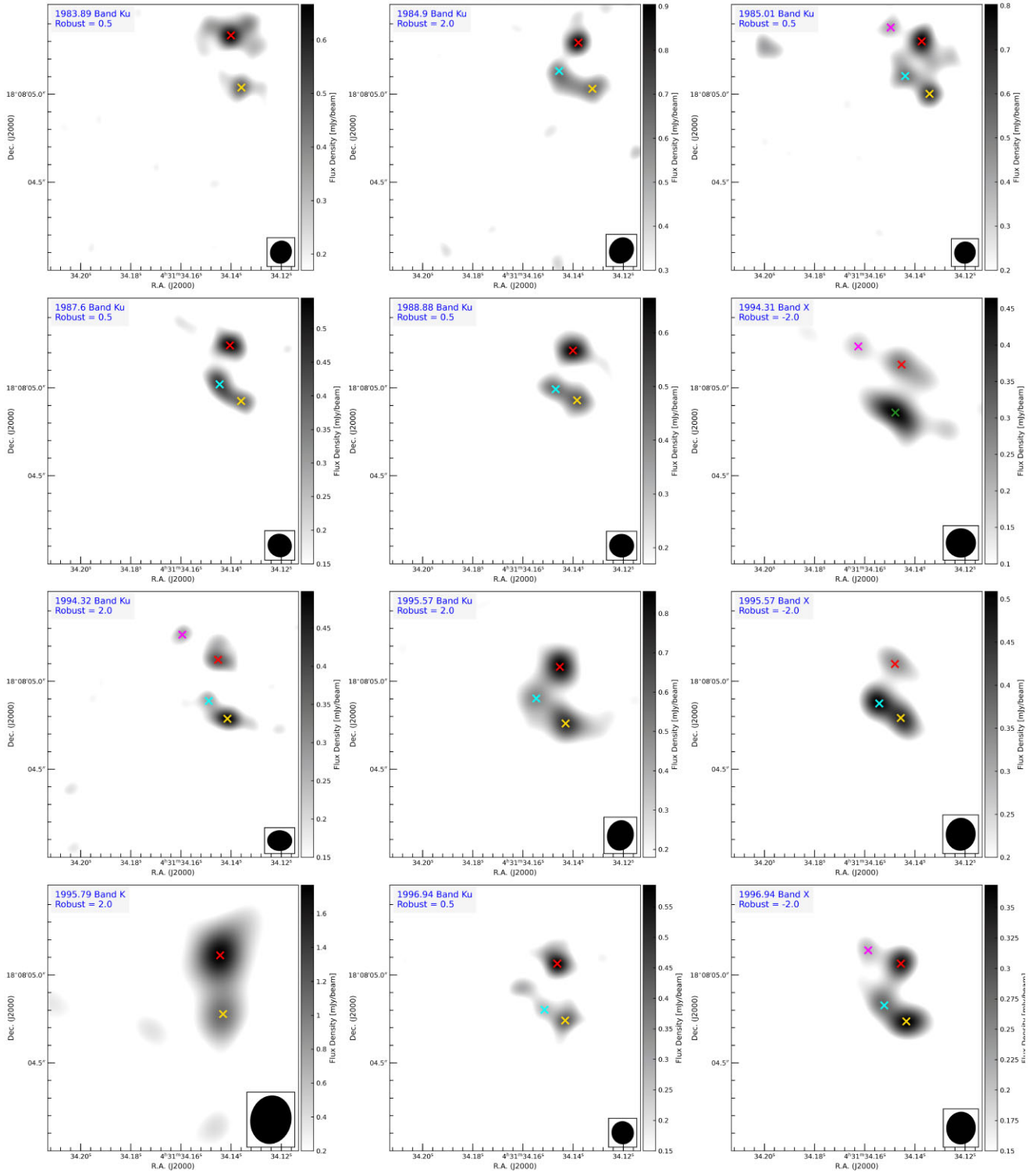


Figure A1. VLA images of all the epochs considered in this paper. The band, epoch, and weighting scheme is indicated at the top left corner in each case and the synthesized beam are shown near the bottom right corner. Red, yellow, magenta, and cyan crosses indicate the measured positions of L 1551 IRS 5 N, L 1551 IRS 5 S, Sh-N, and Sh-S, respectively. When L 1551 IRS 5 S and Sh-S could not be resolved, we measured the position of the elongated resulting source, and indicate it as a green cross.

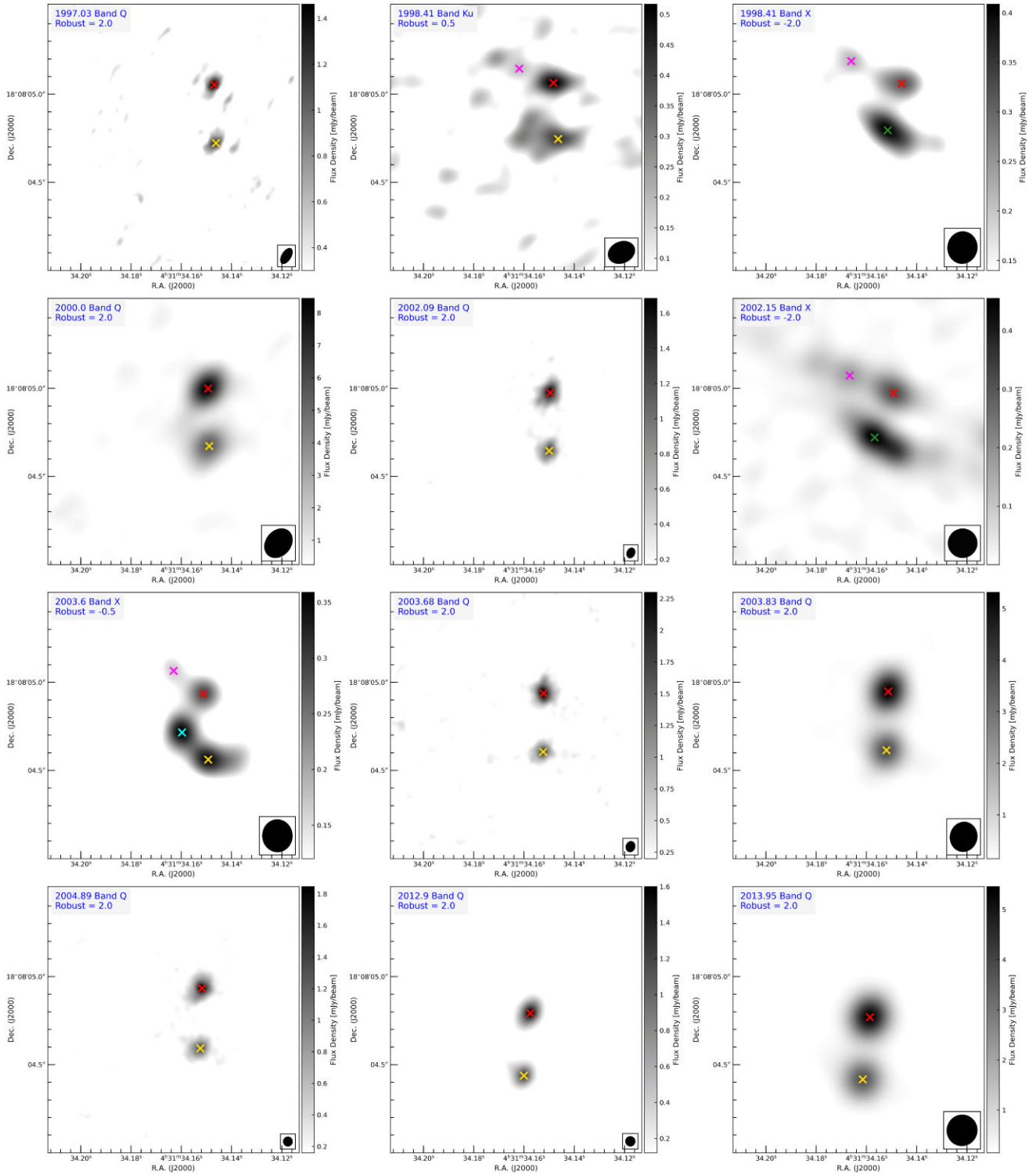


Figure A1. – continued

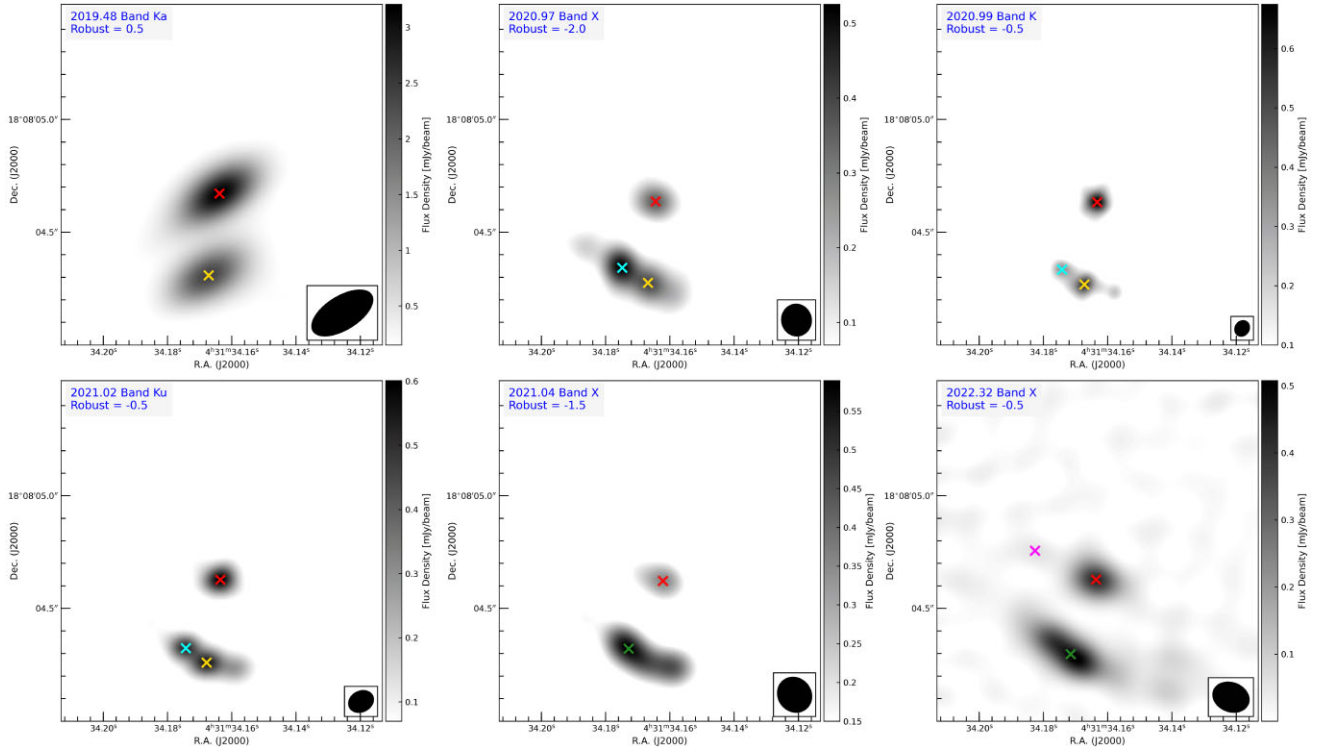


Figure A1. – continued

APPENDIX B: EFFECTS OF THE CORRECTIONS ON THE ABSOLUTE PROPER MOTIONS

Figs 1 and 2 in the main text show the positions of the sources in the L 1551 IRS 5 system as a function of time, after the corrections for the catalogued calibrator position and the trigonometric parallax are applied (see Section 2.2). Figs B1 and B2 in this appendix show the equivalent of Fig. 1, respectively, before any correction is applied, and after only the calibrator corrections are applied. A quick comparison between Figs B1 and 1 clearly shows that the corrections for the catalogued position of the gain calibrators can be substantial, particularly for older VLA data. The parallax corrections are, comparatively, much smaller. These conclusions can be observed quantitatively in Table 4 which shows that the reduced χ^2 improves by factors of 6 and 2 (in right ascension and declination, respectively)

after applying the calibrator corrections. The improvement on the χ^2 after applying the parallax correction is only about 5 per cent, but systematic.

In Fig. B1, we also show, as green squares, the positions reported by Villa et al. (2017). Within the errors, these positions coincide well with our own measurements before applying any correction. We conclude that the reason Villa et al. (2017) obtain inconclusive absolute proper motion measurements is that they did not correct for the catalogued calibrator position changes. This had a particularly adverse effect on their results because two of their six observations were affected by strong positional offsets. We note, finally, that the early Ku band observations reported here were also affected by large catalogued position errors, but that the publications using these data for absolute astrometry (Rodríguez et al. 2003a; Lim & Takakuwa 2006) did incorporate the relevant corrections.

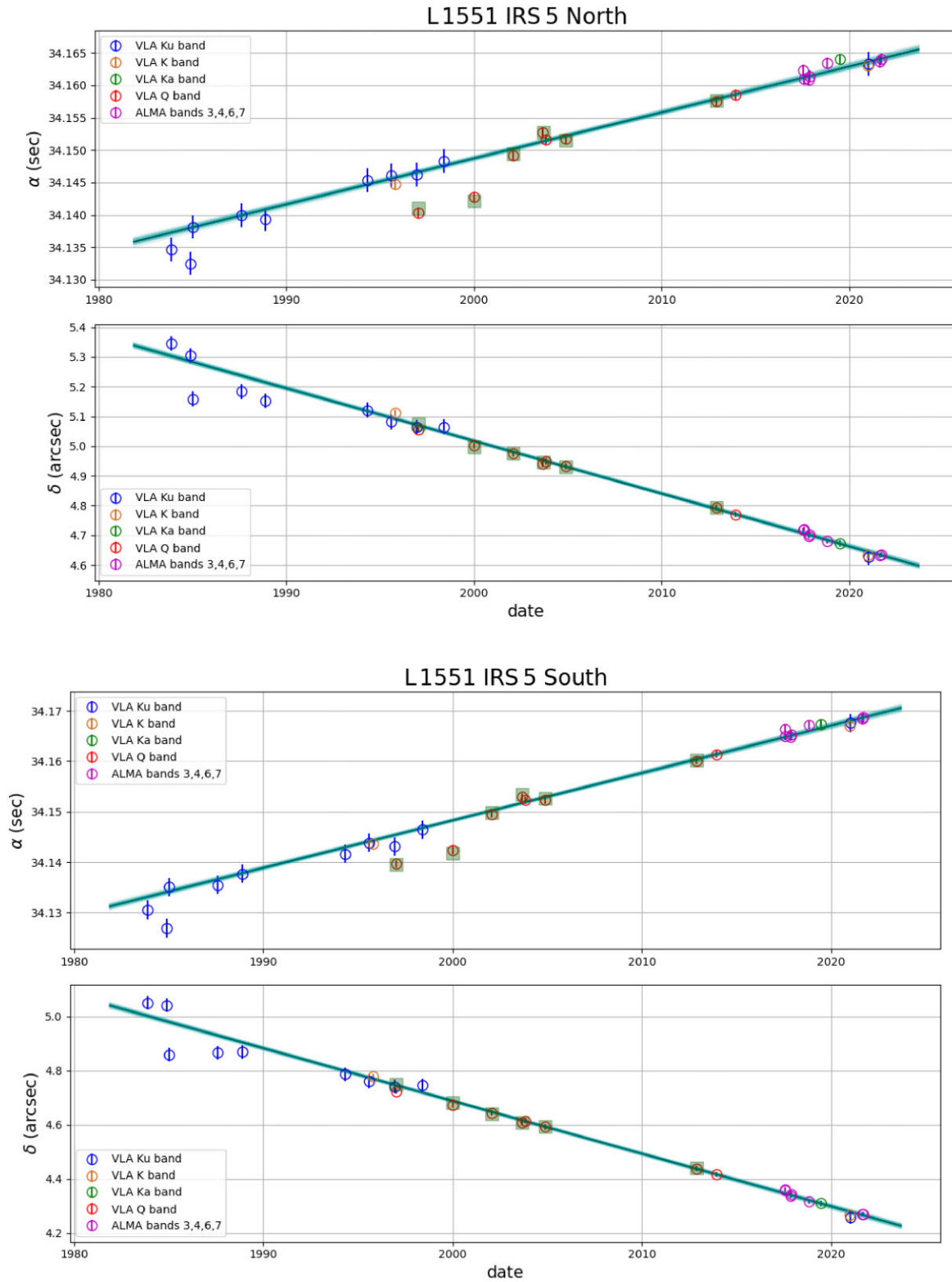


Figure B1. Same as Fig. 1 in the main text but before applying any correction. The indigo squares are the positions reported by Villa et al. (2017). As can be seen, they correspond with our positions before corrections. The fits are the same as in Fig. 1.

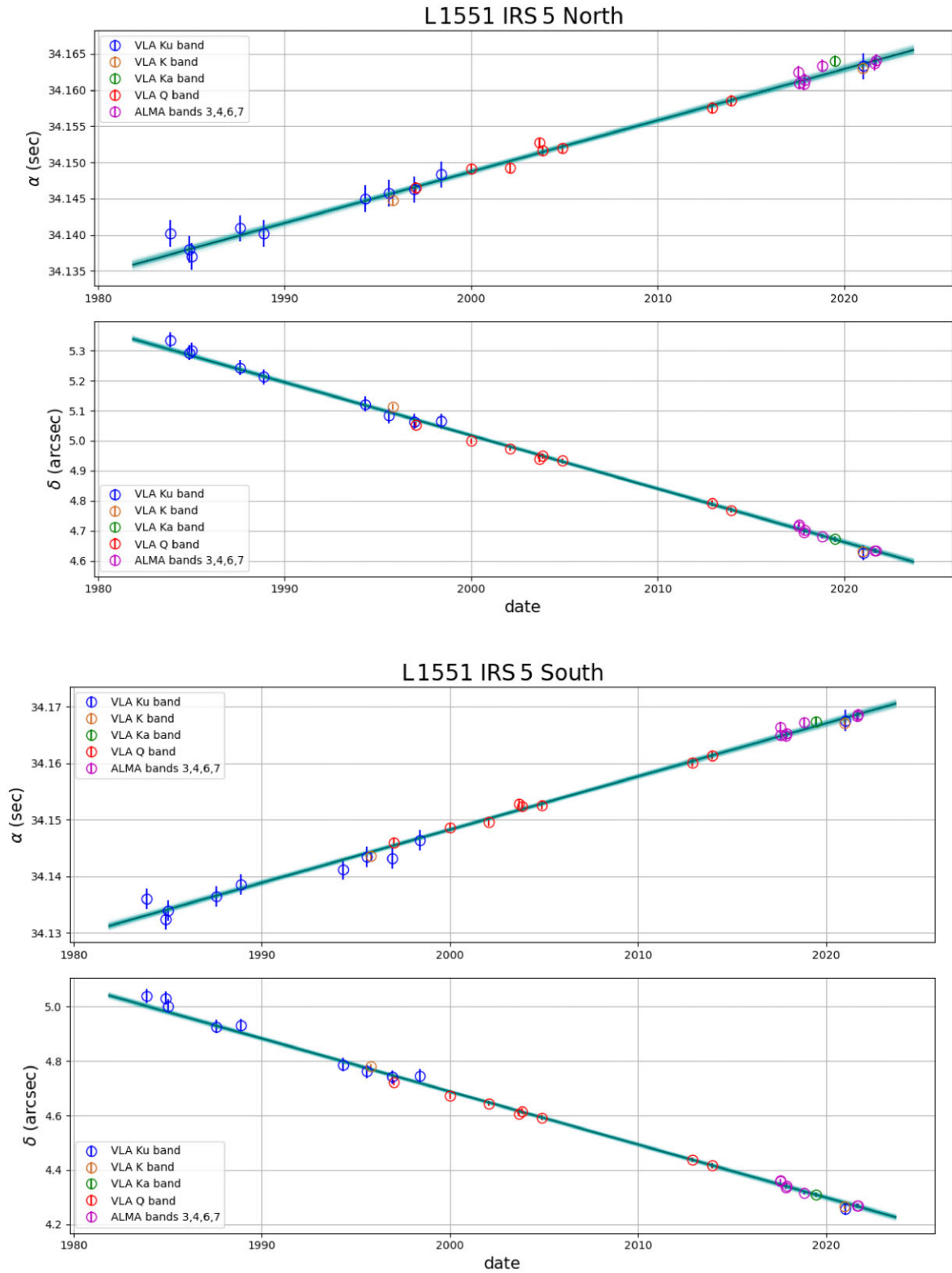


Figure B2. Same as Fig. 1 and B1 after applying the calibrator position corrections, but before applying the parallax corrections. The fits are the same as in Fig. 1.

This paper has been typeset from a \LaTeX file prepared by the author.